Title: Integrative analysis of patient-derived tumoroids and ex vivo organoid modeling of ARID1A loss in bladder cancer reveals therapeutic molecular targets

Authors: Mathijs P. Scholtes[1#], Maryam Akbarzadeh[1,2,3#], J. Alberto Nakauma-Gonzáles[1##], Alexandros Galaras[4,5##], Ameneh Bazrafshan[2##], Bram Torenvliet[2], Leila Beikmohammadi[2,3], Valeria Lozovanu[2], Shahla Romal[2], Panagiotis Moulos[4,5], Tsung Wai Kan[1,6], Mahesh Algoe[6], Martin E. van Royen[6], Andrea Sachetti[6], Thierry P.P. van den Bosch[6], Bert Eussen[7], Annelies de Klein[7], Geert J.L.H. van Leenders[6], Joost L. Boormans[1], Pantelis Hatzis[4], Robert-Jan Palstra[1,2,6], Tahlita C.M. Zuiverloon[1]*, Tokameh Mahmoudi[1,2.6*]

Affiliations:

[1]Department of Urology, Erasmus MC Cancer Institute, University Medical Center Rotterdam, Rotterdam, the Netherlands

[2]Department of Biochemistry, Erasmus MC, University Medical Center Rotterdam, Rotterdam, the Netherlands

[3]Stem Cell and Regenerative Medicine Center of Excellence, Tehran University of Medical Sciences, Tehran, Iran

[4]Institute for Fundamental Biomedical Research (IFBR), Biomedical Sciences Research Center "Alexander Fleming"

[5]Department of Biochemistry and Biotechnology, University of Thessaly, Larissa, Greece

[6]Department of Pathology, Erasmus MC Cancer Institute, University Medical Center Rotterdam, Rotterdam, the Netherlands.

[7]Department of Clinical Genetics, Erasmus MC, University Medical Center Rotterdam, Rotterdam, the Netherlands

[#] equal author contribution

[##]equal author contribution

*To whom correspondence should be addressed: t.mahmoudi@erasmusmc.nl and t.zuiverloon@erasmusmc.nl

ABSTRACT

Somatic mutations in *ARID1A* (AT-rich interactive domain-containing protein 1A) are present in approximately 25% of bladder cancers (BC) and are associated with poor prognosis. With a view to discover effective treatment options for ARID1A-deficient BC patients, we set out to identify targetable effectors dysregulated consequent to ARID1A deficiency. Integrative analyses of ARID1A depletion in normal organoids and data mining in publicly available datasets revealed upregulation of DNA repair and cell cycle-associated genes consequent to loss of ARID1A and identified *CHEK1* (Checkpoint kinase 1) and chromosomal passenger complex member *BIRC5* (Baculoviral IAP Repeat Containing 5) as therapeutically drug-able candidate molecular effectors. *Ex vivo* treatment of patient-derived BC tumoroids with clinically advanced small molecule inhibitors targeting *CHEK1* or *BIRC5* was associated with increased DNA damage signalling and apoptosis, and selectively induced cell death in tumoroids lacking ARID1A protein expression. Thus, integrating public datasets with patient-derived organoid modelling and ex-vivo drug testing can uncover key molecular effectors and mechanisms of oncogenic transformation, potentially leading to novel therapeutic strategies. Our data point to ARID1A protein expression as a suitable candidate biomarker for the selection of BC patients responsive to therapies targeting BIRC5 and CHEK1.

Keywords: *ARID1A*, bladder cancer, BC tumoroids, normal bladder organoids, targeted therapy

INTRODUCTION

Bladder cancer (BC) represents a significant global health burden, ranking as the 12th most prevalent malignancy worldwide and accounting for approximately 200,000 annual deaths[1]. Non-muscle invasive BC (NMIBC) patients have a favourable prognosis and receive local treatment. Management of muscle-invasive BC (MIBC), however, remains challenging due to its propensity for metastasis[2]. Standard-of-care in non-metastatic MIBC patients is cisplatin-based pre-operative chemotherapy and a radical cystectomy (RC)[2]. Despite the toxic side effects of pre-operative chemotherapy, half of MIBC patients will progress to metastatic urothelial cancer (mUC), which is characterized by a 5-year survival rate of approximately 5% [2, 3]. Poor mUC survival outcome highlights the clinical need for additional treatment options.

BC represents an example of how chromatin misregulation leads to cancer[4]. More than 80% of patients with BC harbour cancer-associated mutations in chromatin remodelling genes[4]. One of the most frequently mutated chromatin remodellers in MIBC and mUC is the AT-rich interactive domain-containing protein 1A (*ARID1A*), the defining component of the BAF ATP-dependent SWI/SNF nucleosome remodelling complex[4, 5]. Somatic mutations in *ARID1A* are present in approximately 20-30% of cases of MIBC and mUC, and predominantly include nonsense, point, and insertion or deletion frameshift mutations[4, 6, 7]. These mutations typically result in truncated proteins or reduced protein expression[8]. *ARID1A* is classified as a tumor suppressor because its genetic deletion impairs DNA double-strand break repair, disrupts telomere cohesion, and results in the upregulation of oncogenes[9-12]. The role of *ARID1A* as a global chromatin conformation regulator underlies the diverse effects observed when this gene is disrupted. Cellular processes impaired by loss of *ARID1A* serve as therapeutic targets for *ARID1A*-deficient BC[8, 11, 12]. Pharmacological inhibition of such targets could enable therapies which both exploit tumor-specific gene alterations and reduce overall toxicity.

Although many novel targets are pre-clinically identified for BC, few therapies are implemented in clinical practice. A major bottleneck is the lack of patient-representative preclinical models for candidate drug discovery and validation of clinically effective treatments[13, 14]. Recently, patient-derived tumoroids (malignant) and organoids (non-malignant) have been shown to be robust *ex vivo* platforms that recapitulate many attributes of human tissues, including 3-dimensional structure, multilineage differentiation, histological features, functional characteristics, and patient-treatment responses[15-20]. Additionally, their capacity for genetic manipulation makes tumoroids and organoids an ideal platform for pre-clinical BC research[18-21].

In this study, we explored novel pre-clinical treatment options for *ARID1A*-deficient BC. Our analysis of publicly available sequencing data from MIBC and mUC revealed that genetic aberrations in *ARID1A* are associated with reduced gene expression and poor patient prognosis. Next, we established and characterized a patient-derived BC tumoroid and normal urothelial organoid biobank and utilized this platform to identify dysregulated cellular processes and therapeutic candidate genes consequent to *ARID1A* deficiency. Finally, we investigated *BIRC5* and *CHEK1* as potential pharmacological targets to selectively eliminate ARID1A-deficient BC tumoroids.

RESULTS

ARID1A mutations correlate with reduced *ARID1A* gene expression and poor outcome in MIBC patients

ARID1A is the defining component of the BAF ATP-dependent SWI/SNF nucleosome remodelling complex. In some types of cancer, e.g. ovarian cancer, both deletions and heterozygous truncating mutations result in BAF-complex destabilization and loss of ARID1A protein expression[22]. When evaluating the TCGA MIBC dataset[4], we demonstrated lower ARID1A protein levels in *ARID1A* mutated tumors (P = 0.03, two-sided Wilcoxon-rank sum test), and in tumors harboring *ARID1A* deletions (P = 0.08, two-sided Wilcoxon-rank sum test) (Figure 1A). In addition, positive correlations were detected between ARID1A protein expression, mRNA expression, and copy number status (Supplemental Figure 1A-D).

We did not observe overall survival (OS) differences when patients were stratified based on *ARID1A* somatic mutation status (p = 0.19, log-rank test) (Figure 1B). However, OS was associated with ARID1A expression at the protein level. Patient stratification into three groups based on ARID1A protein expression (low, medium, high), revealed the shortest OS in patients with low ARID1A protein expression (17.7 months), followed by patients with intermediate expression (22.5 months), while the longest OS was observed in patients with high ARID1A-expressing tumors (59.3 months) ($p < 0.05$, log-rank test) (Figure 1C), suggesting that attenuated ARID1A protein expression may represent the most clinically relevant indicator of *ARID1A* deficiency. ARID1A protein expression status was associated with worse outcome regardless of treatment, tumor stage, age, or gender (Supplemental Figure 1E). These analyses, highlight the clinical need to develop alternative treatment options for *ARID1A*-deficient patients, who have a poor outcome with current standard of care treatment.

Given *ARID1A*'s association with DNA-repair, we explored whether *ARID1A* mutation status associated with tumor mutational burden. First, we investigated whole-genome DNA sequencing data of an mUC cohort from the Hartwig Medical Foundation (HMF). In this HMF dataset, the number of single-nucleotide

variants (P=0.44, two-sided Wilcoxon-rank sum test), indels (P=0.73, two-sided Wilcoxon-rank sum test), or multi-nucleotide variants (P=0.67, two-sided Wilcoxon-rank sum test) per megabase did not differ with respect to *ARID1A* mutation status (Supplemental Figure 1F). Strikingly, when evaluating gross chromosomal aberrations, we found *ARID1A* deletions to be associated with lower overall ploidy (P<0.001, two-sided Wilcoxon-rank sum test), fewer genes affected by copy-number alterations (P<0.001, two-sided Wilcoxon-rank sum test), and fewer structural variants (P=0.056, two-sided Wilcoxon-rank sum test), when compared to *ARID1A* wild type status (Figure 1D). Although whole-genome sequencing data from the HMF cohort offers higher resolution to detect aneuploidy at the gene level than microarrays[23], we observed a similar trend in the TCGA cohort. In the TCGA dataset, patient tumors with low ARID1A protein expression had lower overall ploidy (P=0.057, two-sided Wilcoxon-rank sum test), and fewer genes affected by copy-number alterations (P=0.0063, two-sided Wilcoxon-rank sum test), compared to tumors with ARID1A expression (Figure 1E). Although counterintuitive, these results align with a previous study which demonstrated that *ARID1A* inactivation impairs genome maintenance to such extent that *ARID1A*-deficient cancer cells are vulnerable to DNA double-strand breaks during mitosis, resulting in selective elimination of clones that accumulate too much DNA-damage while dividing [24]. However, the molecular mechanisms underlying the observed prognostic and mutational differences associated with ARID1A status in BC have yet to be elucidated with functional studies.

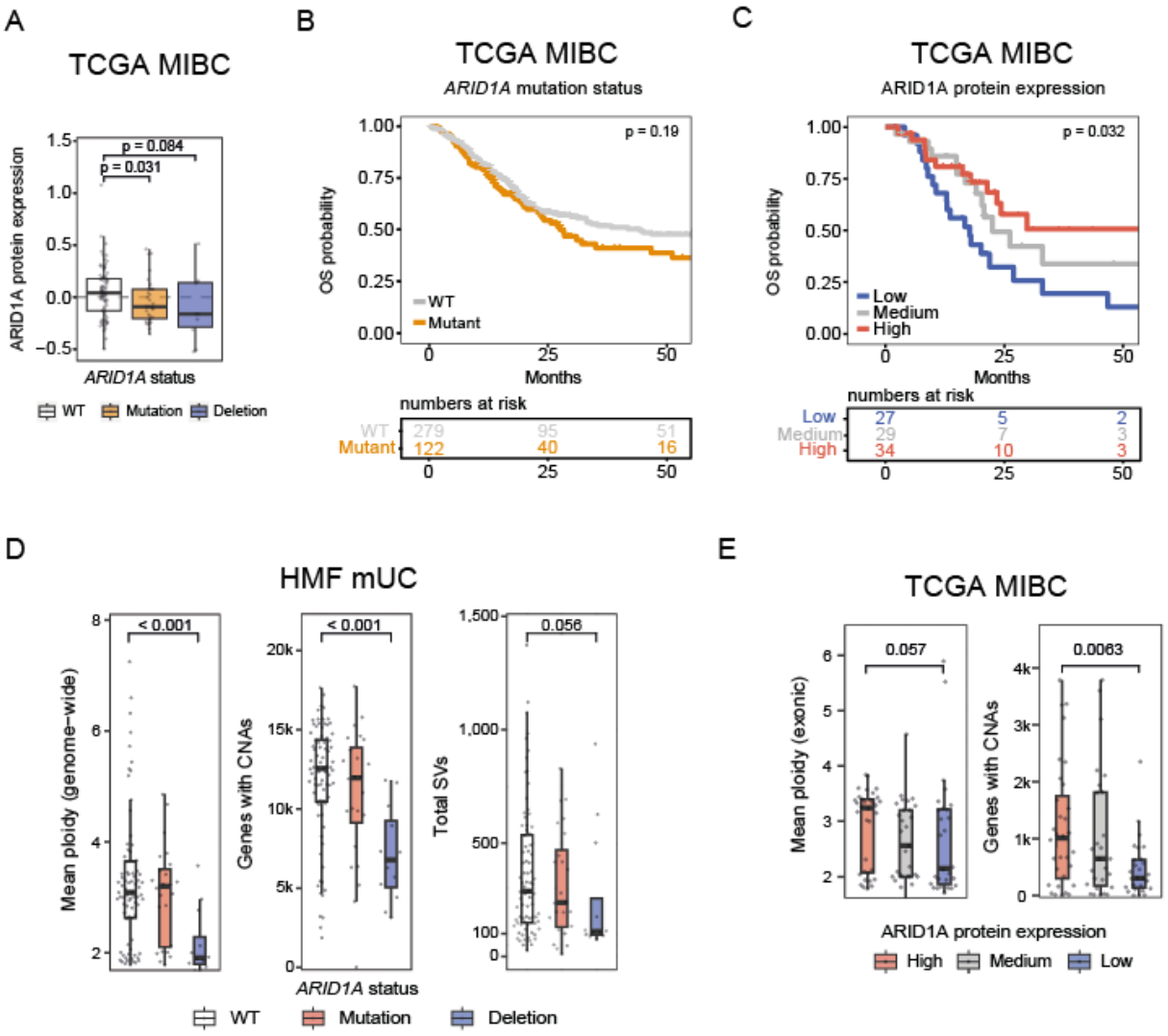

Figure 1. Genetic *ARID1A* aberrations are associated with loss of gene-expression and poor prognosis in MIBC. A) Box plots showing ARID1A protein expression levels quantified by reverse phase protein array (RPPA) in *ARID1A* wild type, mutated and deleted tumors*. A two-sided Wilcoxon-rank sum test was applied. Box plots show the median, inter-quartile range (IQR: Q1–Q3) and whiskers (1.5xIQR from Q3 to the largest value within this range or 1.5xIQR from Q1 to the lowest value within this range). WT = *ARID1A* wild type, Mutation = coding mutations (excluding synonymous) and small insertions/deletions, Deletion = *ARID1A* deleted. **B)** Overall survival curves of n = 401 MIBC patients treated with radical cystectomy*. Patients were stratified by *ARID1A* mutation status. WT = *ARID1A* wild type, Mutant includes protein-coding mutations, small insertions/deletions, and *ARID1A* deletions. The log-rank test was applied to survival curves. **C)** Overall survival curves of n = 90 MIBC patients (one patient excluded with no survival record) treated with radical cystectomy*. Patients were stratified by tertiles of ARID1A protein expression levels (low, medium, high) as determined by RPPA and samples with protein-coding mutations were excluded. The log-rank test was applied to survival curves. **D)** Boxplots depicting mean ploidy, number of genes affected by copy-number aberrations (CNAs) and number of structural variants (SV) in metastatic urothelial cancer samples**. WT = *ARID1A* wild type, Mutation = protein coding mutations (excluding

synonymous) and small insertions/deletions, Deletion = *ARID1A* deleted. Two-sided Wilcoxon-rank sum test was applied. **E)** Boxplots graphs depicting mean ploidy and number of genes affected by copy-number aberrations (CNAs) in MIBC patients stratified by ARID1A protein expression*. Two-sided Wilcoxon-rank sum test was applied. WT = *ARID1A* wild type, Mutation = protein-coding mutations (excluding synonymous) and small insertions/deletions, Deletion = *ARID1A* deleted. *TCGA **HMF.

Biobank of patient-derived BC tumoroid and normal urothelial organoid models that phenotypically and genetically resemble the tissue of origin.

To investigate the impact of ARID1A status on BC in a clinically relevant BC model system, we generated *ex vivo* cultures from BC and macroscopic normal urothelium acquired from BC patients undergoing transurethral resection of bladder tumor (TURBT) or radical cystectomy (Supplemental Figure 2A-C). Patient-derived tumoroid (PDT) and normal organoid (NO) lines were initiated from a variety of BC patients, ranging from low-grade non-invasive NMIBC to high-grade MIBC (Supplemental Figure 2B,D, Supplemental Table 1). Approximately 80% of initiated cultures could be expanded and were successfully cryopreserved (Supplemental Figure 2E-F).

Genome-wide copy-number aberrations (CNA), and hotspot mutation analysis (SNaPshot[25-27]) of the telomerase reverse transcriptase (*TERT*) promoter region and protein-coding regions of Phosphatidylinositol-4,5-Bisphosphate 3-Kinase Catalytic Subunit Alpha (*PIK3CA*) and Fibroblast Growth Factor Receptor 3 (*FGFR3)* confirmed that BC tumoroids and non-malignant bladder organoids genetically resembled their corresponding parental tissues *ex vivo* (Figure 2A-C, Supplemental Figure 3A-B). Additionally, *ex vivo* cultures resembled patient tumor and normal tissue urothelial differentiation marker expression and morphological growth patterns (Figure 2D & Supplemental Figure 3C-D).

Unsupervised hierarchical clustering of 3’ mRNA-seq data of BC tumoroid and normal bladder organoid cultures (n = 34) identified three expression subtypes, highlighted by the five most differentially expressed genes (Figure 2E, Supplemental Figure 4A-B). Cluster one contained tumoroids and normal organoids

169 showing a basal/squamous gene expression signature, whereas cluster two seemed enriched for
170 tumoroids and organoids with a luminal expression signature and presence of activating *FGFR3* mutations.
171 The third cluster exclusively consisted of tumoroids and was characterized by low expression of luminal
172 genes and an epithelial-to-mesenchymal transition (EMT)-associated expression signature.

173

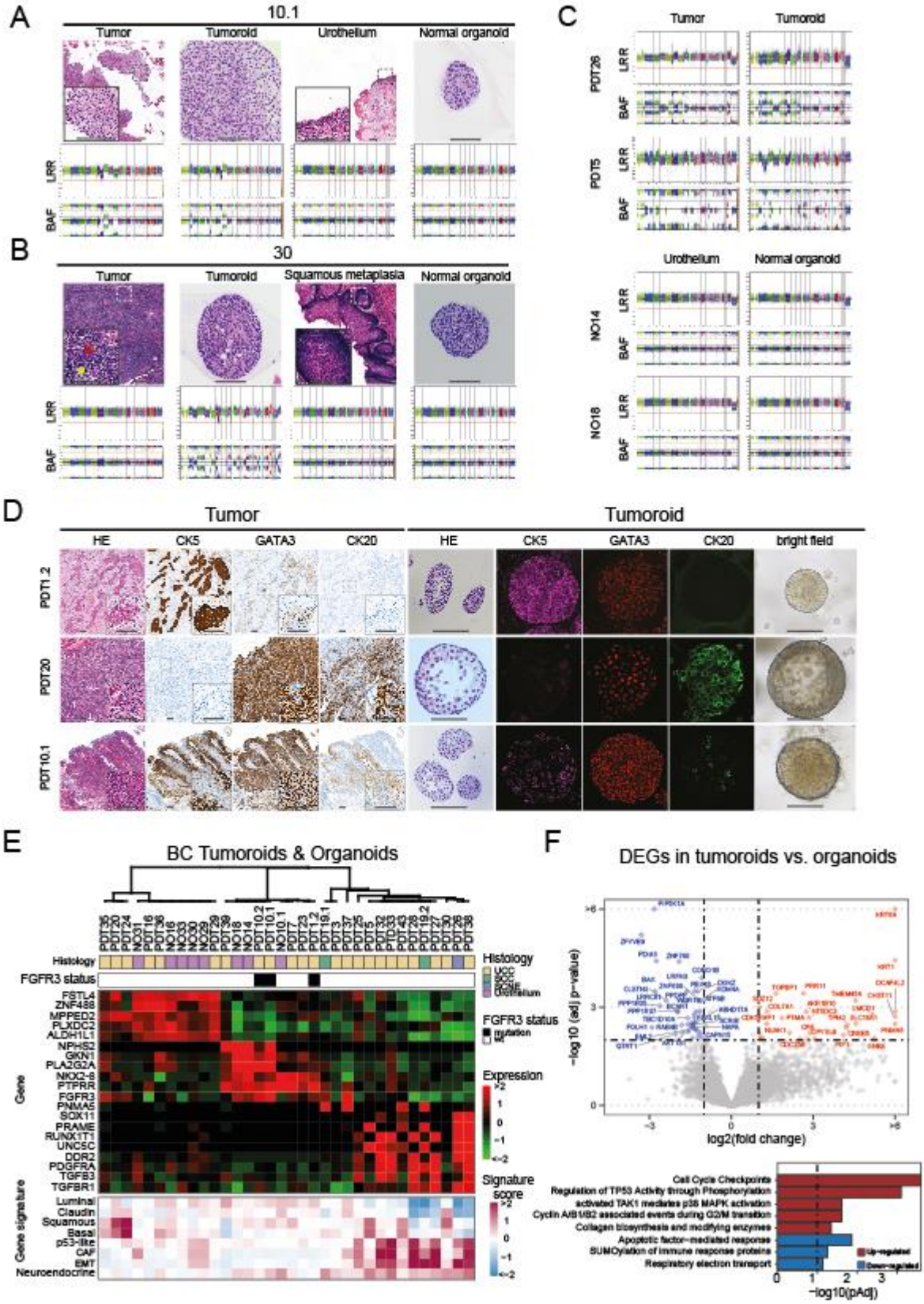

174

Figure 2. Genetic and phenotypic characterization of a BC tumoroid and normal urothelial organoid biobank. A) Top: H&E stainings of patient #10 tissues and corresponding PDTs and NOs (scale bar = 50 µm). Bottom: Scatterplots illustrating genome wide copy number alterations depicted by Log R ratios (LRR) and B-allele frequency (BAF) from #10 tumor (first left), tumoroids (second left), normal urothelium (second right), and normal organoids (first right) **B)** Top: H&E stainings patient #30 tissues and corresponding PDTs and NOs. Red arrow indicates tumor cells, yellow arrow indicates tumor infiltrating lymphocytes (scale bar = 50 µm) Botom: Scatterplots illustrating genome wide copy number alterations from patient #30 tumor (first left), tumoroids (second left), squamous metaplasia (second right), and normal organoids (first right). Note that copy-number alterations (CNAs) are masked in this lymphoepithelioma-like tumor due to high lymphocyte infiltration, but become apparent as CNA resolution increases in the tumoroids. **C)** Scatterplots illustrating genome wide copy number alterations depicted by Log R ratios (LRR) and B-allele frequency (BAF) from patient tumor and corresponding tumoroids (top) or urothelium and corresponding normal organoids (bottom). **D)** Histological evaluation of primary tumors and corresponding tumoroids. Expression of urothelial differentiation markers was investigated by IHC (tumors) and IF (tumoroids) as indicated. Representative examples of basal (PDT1.2; CK+, CK20-), luminal (PDT20; CK5-, CK20+) and mixed basal/luminal (PDT10.1 CK5+, CK2-+) tumor types are shown. (scale bar = 50 µm). **E)** Unsupervised clustering of transcriptomic profiles from patient-derived tumoroids (PDTs) and normal organoids (NOs) identified three clusters (Euclidean distance, Ward method), which are displayed in the dendrogram. Differential gene expression analysis was applied for each group and expression of the top five genes with the highest log2 fold change and adjusted $p < 0.001$ were shown in the heatmap, together with FGFR3, TGFB3, TGFBR1, PDGFRA and DDR2. Additionally, histological subtypes, FGFR3 mutation status and gene expression signatures of patient-derived tumoroid and normal organoid lines are displayed. Histology represents urothelial cell carcinoma (UCC), small cell neuroendocrine-like (SCNE), squamous cell carcinoma (SCC) and normal urothelium. Tumors with somatic mutations in FGFR3 identified by SNaPshot mutation analysis are indicated in black. Gene signature scores represent the average expression of genes associated with each signature. **F)** Volcano plot of differentially expressed genes obtained from RNA sequencing analysis of tumoroid compared to bladder organoids. Genes that were differentially regulated in tumoroids with adjusted $p < 0.01$ and absolute log2 fold change >1 are labeled in red (upregulated) and blue (downregulated), (top). Bar diagrams specify the pathways of differentially expressed genes (adjusted $p < 0.05$, absolute log2 fold change > 0.5) according to the hypergeometric distribution calculated with ReactomePA (adjusted $p < 0.05$, bottom). P values were adjusted with the Benjamini-Hochberg method.

Differential gene-expression analysis of BC tumoroids and normal organoid cultures identified pathways that reflect several hallmarks of cancer and are known to be dysregulated in BC[28]; these include upregulation of pathways involved in MAPK activation, cyclin-associated events during G2/M transition and cell cycle checkpoints (sustaining proliferative signaling), P53 regulation (evading growth

suppressors), and collagen modifying enzymes (activating invasion and metastasis), as well as downregulation of pathways promoting apoptosis (resisting cell death) and respiratory electron transfer (deregulating cellular energetics) (Figure 2F). From the present analysis we conclude that patient-derived BC tumoroids and normal urothelial organoids faithfully represent the tissue of origin.

Loss of *ARID1A* in normal bladder organoids induces upregulation of DNA repair and cell cycle-associated genes

Given the need for novel treatment strategies for patients with loss of ARID1A protein expression, we applied our PDO model to identify potential therapeutic targets that could be exploited in *ARID1A*-deficient BC. Since ARID1A loss has been shown to induce oncogene expression in murine urothelium[29], we investigated which genes are upregulated in response to ARID1A loss in human urothelial cells. Loss of ARID1A expression was modeled by applying short hairpin RNA (shRNA) – mediated ARID1A knock-down in four normal organoid lines (Figure 3A). Efficient *ARID1A* knock-down was confirmed by RT-qPCR (Figure 3B). Thereafter, 3' mRNA-seq and differential gene-expression analysis identified 353 dysregulated transcripts in ARID1A depleted (N=4) compared to matched parental (N=2), or shCTRL (N=2) control organoids (Figure 3C). A total of 247 genes were significantly upregulated, while 106 genes were significantly downregulated. To explore targetable therapeutic approaches, we concentrated on the upregulated genes, as these present opportunities for inhibition with potential drug treatments. Pathway enrichment analysis pointed to significant upregulation of DNA damage repair (DDR) genes such as *ATM*, *RAD51*, *PALB2*, *BRCA1*, *BARD1*, *FANCA*, *FANCI*, and *FANCG*, and genes involved in cell cycle checkpoint and G1 to G1/S phase transition including *CHEK1*, *CHEK2*, *PRC1*, *BIRC5*, *CDCA8* and *AURKB* (Figure 3C-D). Next, we performed a motif enrichment analysis to identify transcription factors underlying the observed transcriptomic changes associated with ARID1A loss. Homer motif analysis predicted only one de novo motif enriched in the transcription start sites (TSS) of upregulated genes with confidence. This motif is

similar to early region 2 factor (E2F) family member binding sites, with the E2F8 binding motif showing the highest resemblance (Figure 3E, Supplemental Figure 5A). The E2F transcription factor family consists of transcriptional activators (E2F1-3) and repressors (E2F4-8) that orchestrate gene-expression in cell cycle regulation and DNA stress response [30-34]. Interestingly, the consensus binding site for the transcriptional repressor E2F8 was found enriched in TSSs of 32 dysregulated genes, of which 25 were upregulated in the ARID1A depleted organoids, pointing to reduction of E2F8 controlled repression upon ARID1A loss (Supplemental Figure 5B). Cross-referencing to publicly available ARID1A CUT&Tag[29] and E2F8 ChIP-seq data[35] demonstrated enrichment of ARID1A and E2F8 binding at the TSSs of genes upregulated by ARID1A knock-down, suggesting a direct link between loss of ARID1A expression and de-repression of E2F8-regulated genes (Figure 3F).

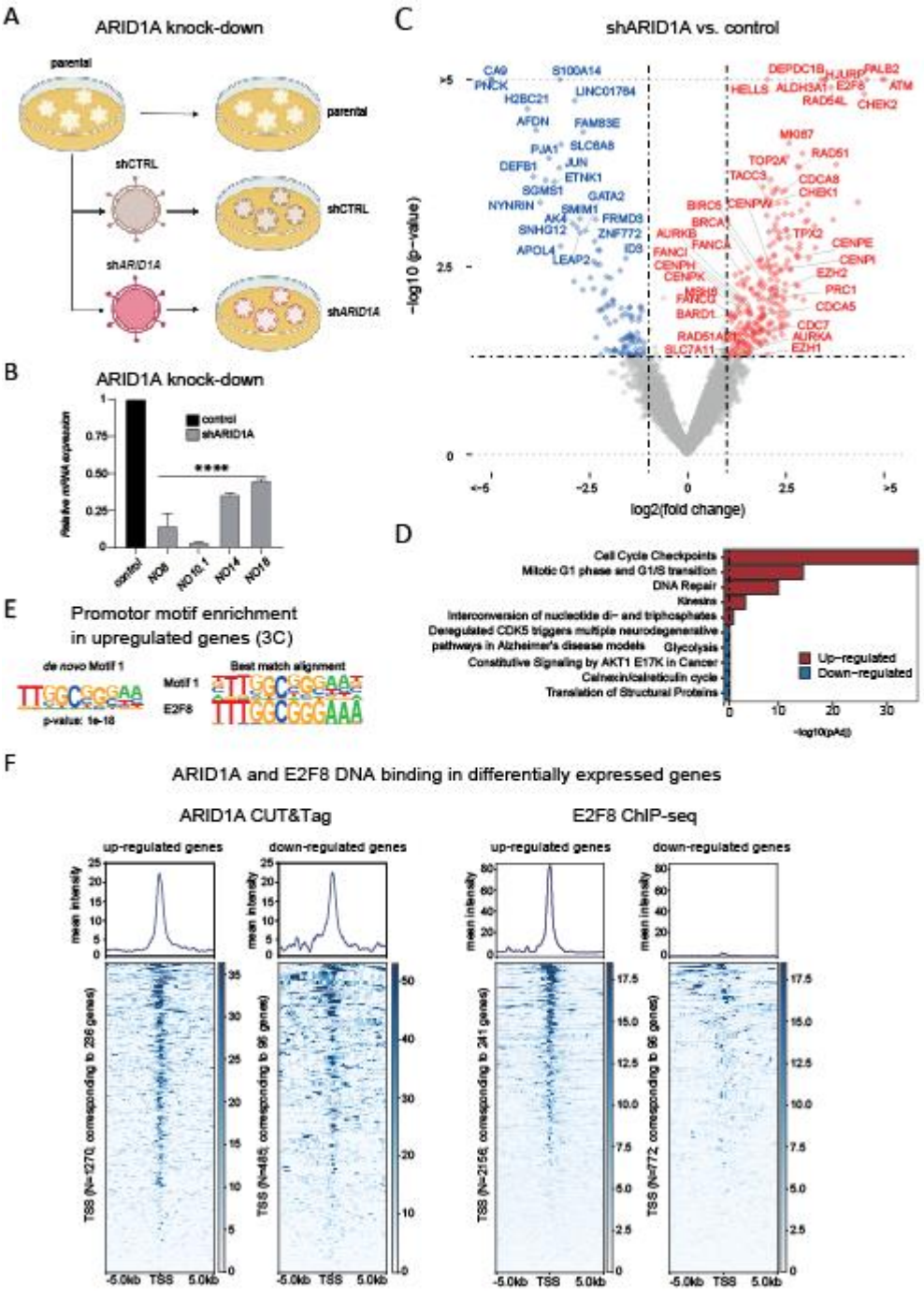

Figure 3. Loss of ARID1A expression in normal bladder organoids induces upregulation of DNA-repair pathways and cell cycle-associated genes A) Schematic representation of the experimental procedure for ARID1A knock-down in urothelial organoids. Following transduction with a lentiviral vector expressing a scrambled shRNA or shRNA targeting *ARID1A* (sh*ARID1A*), organoids were selected with puromycin for 5 days to obtain bladder organoid lines depleted of ARID1A. Four *ARID1A* knock-down (sh*ARID1A*) and corresponding control (shCTRL; NO8 & NO10.1) or untransduced parental (NO14 & NO18) organoid lines were established according to the schematic. **(B)** Levels of *ARID1A* mRNA expression were evaluated by reverse transcription polymerase chain reaction (RT-PCR) in control

(shCTRL; NO8 & NO10.1) or untransduced parental (NO14 & NO18), and the transduced (sh*ARID1A*) bladder organoid lines. Expression of *ARID1A* was calculated according to the 2ΔCt method comparing knock-down vs matched controls, using the housekeeping gene Cyclophillin A as reference. One-way ANOVA comparing knock-down vs. control. *** P<0.0005 **C)** Volcano plot of differentially expressed genes obtained from RNA sequencing analysis of control versus ARID1A depleted bladder organoids as indicated. The expression levels of 353 genes were differentially regulated by ARID1A depletion (up- and down-regulated genes are depicted in red and blue, respectively). The name of selected genes is highlighted. P-values were not adjusted for multiple testing. **D)** Bar graph depicting pathways of the differentially expressed genes according to the hypergeometric distribution calculated with ReactomePA (adjusted $p < 0.05$). **E)** Left: Logo depicting the top *de novo* binding motif (Motif 1), enriched in the promoters of genes upregulated upon ARID1A knock-down (upregulated genes from panel 3C), based on Homer analysis. Right: Logos for predicted Motif 1 and its best match, as determined by sequence alignment (E2F8). **F)** Left: histograms depicting mean ARID1A or E2F8 binding intensities around transcription start sites (TSS) of up- and down-regulated genes as indicated (dysregulated genes from panel 3C). ARID1A CUT&Tag data from murine urothelial organoids was repurposed from Jana et al.[29]. Only genes with murine orthologues (236 out of 247 upregulated genes) are shown. E2F8 ChIP-seq data from K562 (myeloid progenitor was repurposed from the ENCODE project[35]).

Upregulation of chromosomal passenger complex members and cell cycle checkpoint kinases in *ARID1A*-deficient BC

Cell cycle checkpoint-associated genes were the most significantly upregulated gene set in ARID1A-depleted bladder organoids compared to controls (Figure 3D). The same pattern was observed when comparing tumoroids to bladder organoids (Figure 2F), hereby prompting us to focus on cell cycle checkpoint genes. Ensuring clinical relevance, we cross-referenced upregulated genes identified by ARID1A knock-down to genes upregulated in BC patients with *ARID1A* mutated/deleted or low *ARID1A* expressing tumors. First, we investigated which cell cycle checkpoint genes were significantly upregulated in *ARID1A*-deficient MIBC samples from the TCGA cohort. We identified a total of 73 cell cycle checkpoint-associated genes to be significantly upregulated in MIBC tumors with *ARID1A* deletions (1) and low mRNA expression (72) (Supplemental table 2). Comparing this list to the cell cycle checkpoint-genes upregulated in ARID1A-depleted organoids resulted in 16 overlapping candidate genes (Figure 4A). Unsupervised hierarchical clustering using these genes yielded a clear separation between sh*ARID1A* and control

organoids (Figure 4A). Additionally, direct binding of ARID1A and E2F8 was observed at the transcription start sites of the majority of these genes (Supplemental Figure 6). To confirm association of ARID1A status with cell-cycle checkpoint candidate expression, we performed unsupervised hierarchical clustering of the 16 cell-cycle-checkpoint candidate genes on RNA-sequencing data from our patient-derived tumoroids. BC tumoroids separated into two major clusters, suggesting separation by ARID1A status in a manner similar to that observed for ARID1A-depleted organoids (Figure 4B). We randomly selected five BC PDTs from each of the two major clusters and examined ARID1A protein expression using IHC (Figure 4C). IHC identified five BC tumoroid lines with ARID1A expression and five lines without, with eight lines matching the ARID1A status suggested by unsupervised clustering. We then explored whether our 16 cell-cycle-checkpoint candidate genes were also upregulated in *ARID1A*-deficient mUC samples, and whether we could identify *ARID1A*-deficient BC patients by assessing ARID1A protein expression by IHC. For this purpose, we selected samples from the HMF mUC cohort[7, 36] with formalin-fixed paraffin-embedded (FFPE) blocks available for further analysis (N=8). We performed IHC for ARID1A, and summarized *ARID1A* mutation status, ARID1A protein expression and cell-cycle-checkpoint candidate gene mRNA expression into a single heatmap (Figure 4D-E). Unsupervised hierarchical clustering separated the samples into two clearly distinct clusters, one with cell-cycle-checkpoint candidate gene upregulation, and one without. The cluster with upregulation of the 16 cell-cycle-checkpoint candidate genes was enriched for patients with low ARID1A protein expression (Q-score <100, 3 out of 4), *ARID1A* deep deletions (1 out of 4), or *ARID1A* mutations (1 out of 4). Thus, *ARID1A*-deficiency is associated with upregulation of the 16 cell-cycle-checkpoint candidate genes in bladder organoids, BC tumoroids, as well as MIBC and mUC patient tumors.

Three of the identified candidate genes, *BIRC5, CDCA8*, and *AURKB*, form, together with *INCENP*, the chromosomal passenger complex (CPC). The CPC has been described as a master regulator of mitosis, functioning in chromosome–microtubule attachment, activation of the spindle assembly checkpoint, and cytokinesis[37]. The combined mRNA expression of these CPC members was found to be higher in *ARID1A*-

deleted and low *ARID1A*-mRNA expressing MIBC tumors, and in patient tumors with low ARID1A protein expression (Figure 4F). Candidate genes *CHEK1* and *CHEK2* are two functionally—but not structurally—related serine/threonine kinases that are activated in response to DNA damage during mitosis. Upon activation, *CHEK1* and *CHEK2* delay cell cycle progression and facilitate DNA repair until damage has been restored, making *CHEK1* and *CHEK2* interesting candidate genes for further investigation[38]. In addition to CPC members, also *CHEK1* and *CHEK2* were significantly upregulated in *ARID1A*-deleted or low *ARID1A*-mRNA expressing MIBC tumors (Figure 4G). From this analysis, we conclude that ARID1A-deficient BC is associated with the upregulation of CPC members (BIRC5, AURKB, INCENP, and CDCA8) as well as checkpoint kinases (CHEK1 and CHEK2).

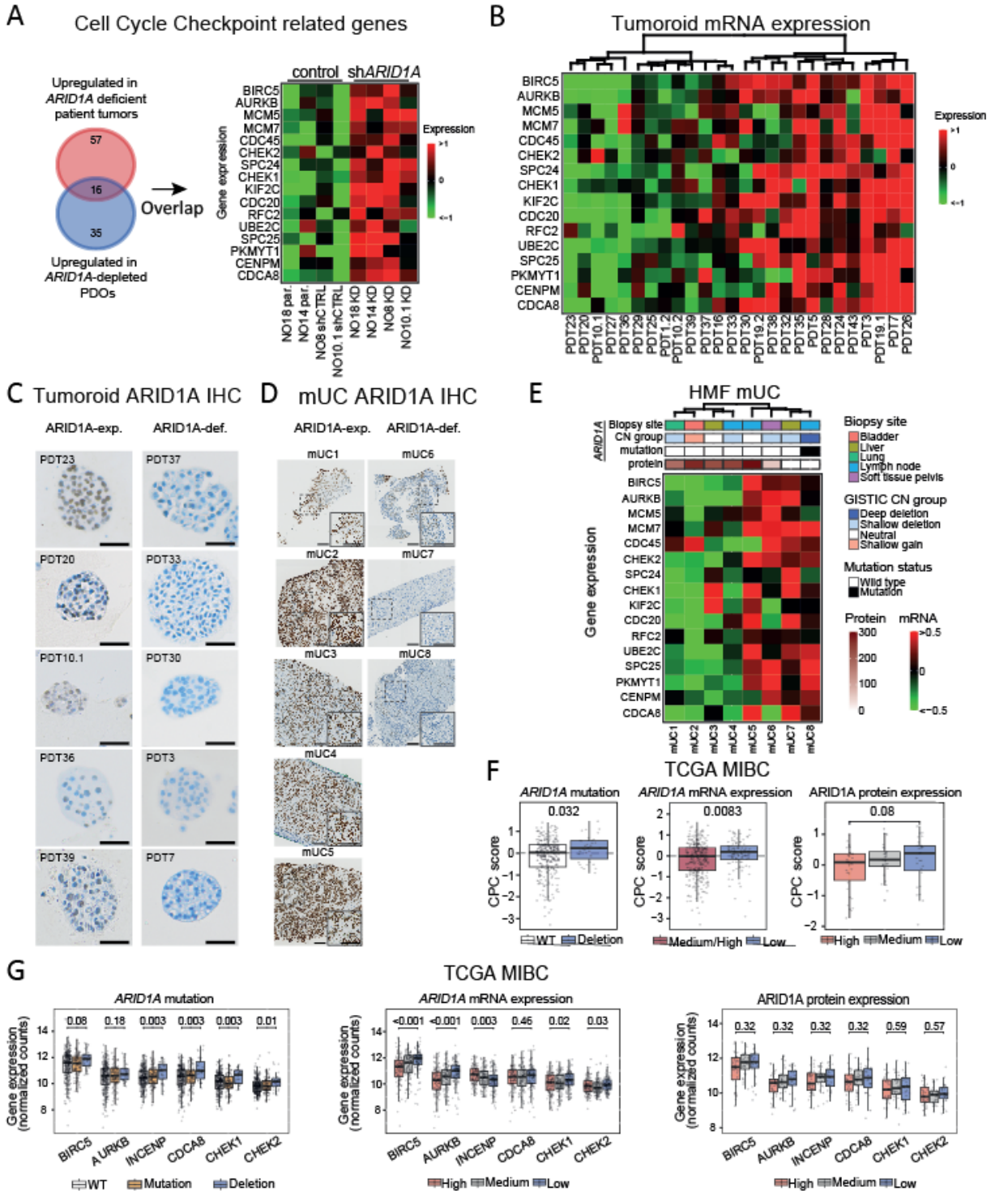

Figure 4. Chromosomal passenger complex members and cell cycle checkpoints are upregulated in *ARID1A*-deficient tumors A) Venn-diagram comparing cell cycle checkpoint genes significantly upregulated in MIBC patient tumors with *ARID1A* deletions or low mRNA* (top) to genes significantly upregulated upon ARID1A depletion in normal urothelial organoids (bottom). Overlapping genes were subsequently used for unsupervised hierarchical clustering (Euclidean distance, Ward method) of ARID1A knock-down (KD), parental (par.) or control (shCTRL) organoid lines. **B)** Heatmap depicting unsupervised

hierarchical clustering of BC patient-derived tumoroids (PDTs) by normalized expression of N = 16 cell cycle checkpoint genes associated with *ARID1A* deficiency. **C)** Representative images of ARID1A immunohistochemistry in PDTs and matched patient tumors. (scale bar = 50 µm). **D)** Representative examples of ARID1A-stained metastatic lesions. (scale bar = 100 µm). **E)** Unsupervised hierarchical clustering (Euclidean distance, Ward method) of N = 8 metastatic BC samples summarizing biopsy sites**, *ARID1A* copy-number status**, *ARID1A* mutations status**, ARID1A protein expression investigated by IHC (Q-score), and = 16 cell cycle checkpoint genes associated with loss of *ARID1A*. Data was repurposed from TCGA (*) or HMF (**) datasets. **F)** Boxplots comparing chromosomal passenger complex (CPC) score integrating *BIRC5*, *AURKB*, *CDCA8*, and *INCENP* mRNA expression in MIBC patient tumors with *ARID1A* wild type vs. deleted tumors* (left), medium/high vs. low *ARID1A* mRNA expression* (middle), and high vs. medium vs. low ARID1A protein expression* (right). Two-sided Wilcoxon-rank sum test was applied to compare differences between the groups. **G)** Boxplots comparing mRNA expression of *BIRC5, AURKB, INCENP, CDCA8*, *CHEK1* and *CHEK2* in MIBC patient tumors stratified by *ARID1A* mutation status* (top), mRNA expression levels* (middle) or protein expression levels* (bottom). Two-sided Wilcoxon-rank sum test was applied and p-values were corrected with the Benjamini–Hochberg method. Box plots show the median, inter-quartile range (IQR: Q1–Q3) and whiskers (1.5xIQR from Q3 to the largest value within this range or 1.5xIQR from Q1 to the lowest value within this range). *HMF, ** TCGA.

Pharmacological *BIRC5* and *CHEK1* inhibition is associated with increased DNA damage signaling in ARID1A-deficient BC.

Next, we investigated the effects of pharmacological inhibition of upregulated candidate genes on cell cycle distribution and DNA-damage signaling in context of ARID1A-deficient BC. Clinically advanced inhibitor drugs are available for *BIRC5* (Baculoviral IAP Repeat Containing 5) and *CHEK1* (Checkpoint Kinase 1). *BIRC5* transcription is inhibited by YM155 (sepantronium bromide), leading to decreased expression of the *BIRC5*-encoded protein survivin[39-42]. CHEK1 kinase activity is inhibited by prexasertib, a drug which was recently given FDA fast-track designation for treatment of ovarian and endometrial cancer patients[43]. To gain mechanistic insight into cell cycle distribution and DNA-damage signaling, we used a flow cytometry approach to explore cell cycle distribution and the presence of DNA-damage, both top enriched pathways revealed by our ARID1A-depletion experiments (Supplemental Figure 7A). Cell cycle distribution was similar between ARID1A-expressing (N=3) and ARID1A-deficient (N=3) tumoroids, and treatment with prexasertib (*CHEK1*) or YM155 (*BIRC5*) did not induce significant changes between the two

359 groups (Figure 5A, Supplemental Figure 7B). DNA-damage signaling (yH2Ax) was similar between
360 untreated ARID1A-expressing (N=3) and ARID1A-deficient (N=3) BC tumoroids; however, prexasertib or
361 YM155 treatment significantly increased DNA-damage signaling in ARID1A-deficient as compared to
362 ARID1A-expressing tumoroids (Figure 5B-C, Supplemental Figure 7B-C).

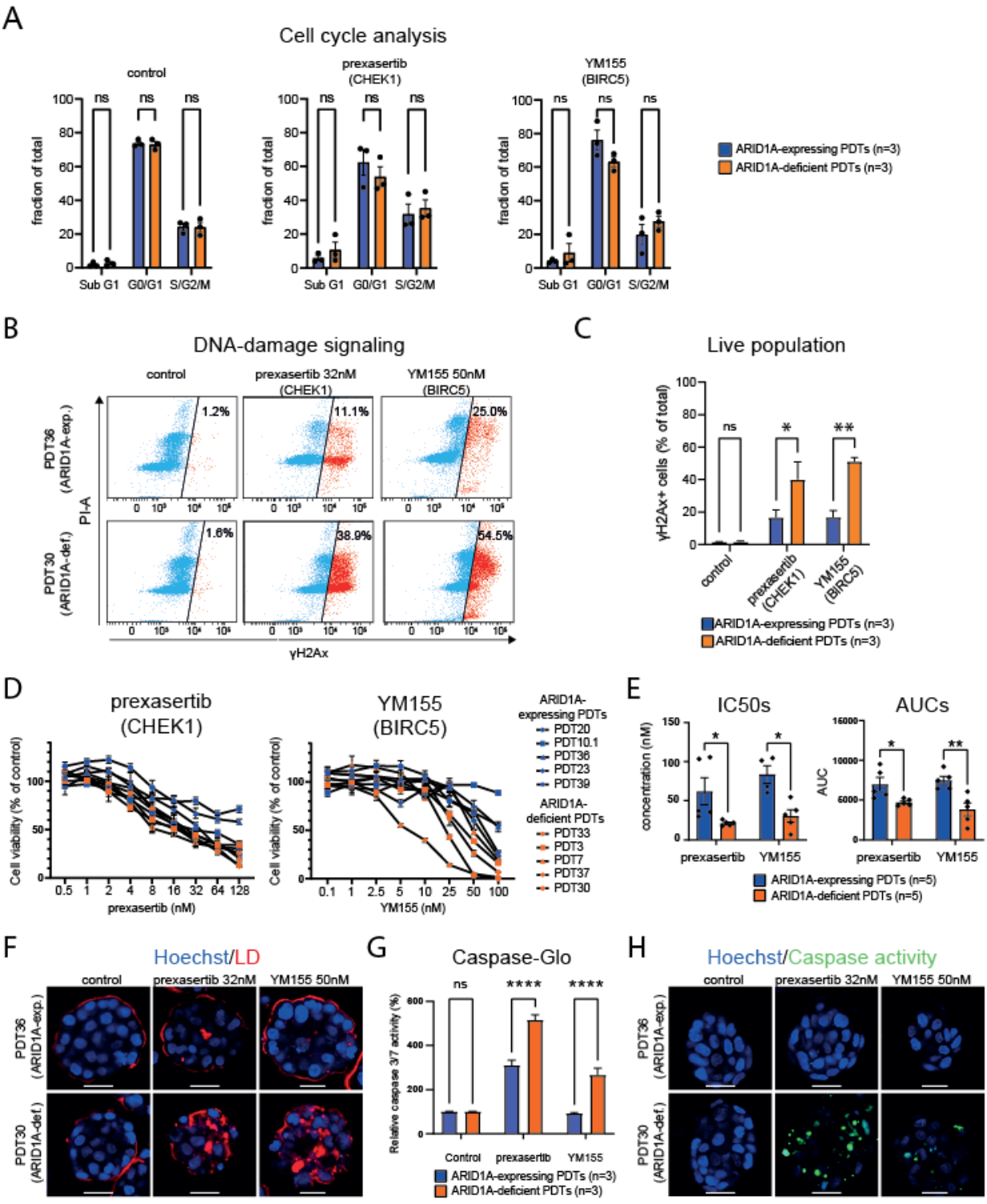

Figure 5. Pharmacological BIRC5 or CHEK1 inhibition selectively targets ARID1A-deficient BC A) Bar graphs summarizing cell cycle distribution of ARID1A-expressing (PDT20, PDT36, PDT39) and ARID1A-deficient (PDT3, PDT30, and PDT37) tumoroids at baseline (untreated control, left), and after treatment with 32nM prexasertib (middle) or 50nM YM155 (right). Data are represented as mean ± SEM. **B)** Flow cytometry of ARID1A-expressing (PDT36) and ARID1A-deficient (PDT30) tumoroids treated with 32nM prexasertib or 50nM YM155 for four days. Gated on the single, live population followed by analysis of

propidium iodide (cell cycle) and phosphorylated H2Ax (yH2Ax) to identify the yH2Ax+ fraction (red). **C)** Bar graphs depicting percentage of yH2Ax cells in ARID1A-expressing tumoroids (PDT20, PDT36, PDT39) and ARID1A-deficient tumoroids (PDT3, PDT30, PDT37), treated with 32nM prexasertib or 50nM YM155 for two days. (mean ± SEM, two-way ANOVA, *p<0.05, **p<0.005). **D)** Dose-response curves for ARID1A-expressing (blue) and ARID1A-deficient (orange) PDTs treated with *CHEK1*-inhibitor prexasertib (left), and BIRC5-inhibitor YM155 (right). Cell viability was measured through CellTiter-Glo 3D. (technical triplicates of two independent experiments; mean ± SEM). **E)** Left: IC50 values estimated from non-linear fit of dose-response depicted in D. YM155 IC50 concentration could not be determined for PDT10.1 due to the line's high resistance. Right: Area under the curve (AUC) of dose-response depicted in D. two-way ANOVA, *p<0.05, ** p<0.005. **F)** Fluorescence staining of ARID1A-expressing (PDT36) and ARID1A-deficient (PDT30) PDTs, treated with 32nM prexasertib or 50nM YM155 for two days. Tumoroids were stained with fixable life/dead staining (LD), nuclei were counter stained with Hoechst. (Scale bar = 25 µm). **G)** Bar graph depicting relative caspase 3/7 activity measured by Caspase-Glo in ARID1A-expressing (PDT20, PDT36, PDT39) and ARID1A-deficient (PDT3, PDT30, PDT37) PDTs following treatment with 32nM prexasertib or 50nM YM155 for two days. (triplicates of two independent experiments; mean ± SEM), two-way ANOVA, ***p<0.0005, ****p<0.00005.) **H)** Fluorescence staining of caspase activity reporter on ARID1A-expressing (PDT36) and ARID1A-deficient (PDT30) PDTs treated with 32nM prexasertib or 50nM YM155 for two days, nuclei were counter stained with Hoechst. (Scale bar = 25 µm).

Selective susceptibility of ARID1A-deficient BC tumoroids to pharmacological inhibition of *BIRC5* or CHEK1

To investigate if CHEK1 and BIRC5 inhibition can selectively kill ARID1A-deficient cancer cells, we treated ARID1A-expressing (N=5) and ARID1A-deficient (N=5) bladder cancer (BC) tumoroids with a concentration range of inhibitors targeting BIRC5 and CHEK1, followed by cell viability and apoptosis assessments. Both YM155 and prexasertib treatment resulted in patient-specific *ex vivo* drug responses as quantified by CellTiter-Glo 3D (Figure 5D). For both drugs, ARID1A-deficient BC tumoroids (N=5) showed significantly lower IC50 values and area under the curve (AUC) compared to ARID1A-expressing (N=5) BC tumoroids (Figure 5E). Furthermore, ARID1A-deficient BC tumoroids (N=1) treated with YM155 or prexasertib exhibited more cell death than ARID1A-expressing tumoroids (N=1) (Figure 5F, Supplemental Figure 8). Additionally, ARID1A-deficient BC tumoroids displayed significantly increased apoptosis following treatment with prexasertib and YM155, compared to ARID1A-expressing BC tumoroids as was determined by a Caspase-Glo 3/7 assay (n=3 for each group, Figure 5G) and visualized by a caspase 3/7 activity reporter

(n=1 for each group, Figure 5H, Supplemental Figure 9). These findings indicate that ARID1A-deficient BC tumoroids are selectively eliminated by YM155 or prexasertib treatment.

To conclude, our ex vivo experiments and patient tumor analyses demonstrate that ARID1A deficiency is associated with the upregulation of E2F8 target genes, including cell cycle-associated genes *BIRC5* and *CHEK1*. In turn, pharmacological inhibition of BIRC5 and CHEK1 via clinically advanced small molecules selectively eliminates *ARID1A*–deficient BC. Our data suggest a promising therapeutic strategy for targeting molecular effectors upregulated due to *ARID1A* deficiency, thereby enhancing the selectivity in eliminating *ARID1A*-deficient BC.

Discussion

Somatic *ARID1A* mutations are detected in approximately 6% of all human cancers [44], with increased frequencies in bladder cancer (~30%)[4], ovarian clear-cell carcinomas (~45%)[22], endometrial carcinomas (~30%) [22], and gastric cancer (~15%)[45]. Novel treatments exploiting specific molecular changes introduced by *ARID1A* deficiency could benefit many cancer patients. Pharmacological strategies that exploit *ARID1A* deficiency include PRIMA-1 treatment to inhibit glutathione synthesis[46], homoharringtonine (HHT) treatment to inhibit protein synthesis [9], and GSK126 treatment to inhibit Enhancer of zeste homolog 2 (*EZH2*), the catalytic subunit of the polycomb repressive complex 2 (PRC2), which is known to functionally antagonize mammalian SWI/SNF complexes [47, 48].

In this study, we utilize bladder organoids to pioneer the first human ARID1A-depleted urothelium model, which RNA-sequencing analysis demonstrated to recapitulate *ARID1A*-mutated human BC; we then used this model system to identify novel therapeutic targets for *ARID1A*-deficient BC patients. Patient-derived organoids and tumoroids have demonstrated their invaluable utility as models for studying tumor biology[17, 49]. They faithfully mirror the *in vivo* characteristics of their native tissues, and, when combined with modern experimental techniques, offer experimental versatility and a robust platform for investigating the molecular underpinnings of bladder cancer[19, 20, 50-52]. Moreover, PDTs have been shown to predict patient treatment response, as shown for colorectal, ovarian, and pancreatic cancer[15, 53-55]. Genetic transformation of human organoids has provided significant mechanistic understanding of oncogenic loci identified through extensive genome sequencing investigations of human malignancies[12, 56-58]. Using this ARID1A-depleted urothelium organoid model we identified significant upregulation of DNA repair genes, genes involved in cell-cycle-checkpoint and G1 to G1/S phase transition. Interestingly, the consensus binding site for the transcription repressor E2F8 was significantly enriched in

the TSSs of the up-, but not in down-regulated genes. This indicates that upregulation of a subset of genes upon ARID1A depletion is (partly) mediated through modulation of E2F8 binding and suggests a model in which ARID1A facilitates binding of E2F8 to its consensus sites to allow transcriptional repression of its target genes (Supplemental Figure 10). This is supported by data from previous studies reporting direct binding of E2F factors by ARID1A[59], ARID1A-dependent repression of E2F-responsive genes[60-62], and E2F8 binding at ARID1A target genes[9, 33, 64]. Many E2F target genes exhibit an oscillatory expression pattern throughout the cell cycle, characterized by low expression during the M/G1 phase, an increase in expression during the G1/S transition, and a decrease during the G2/M phase[63, 64]. E2F target gene expression is orchestrated by transcriptional activators (E2F1-3) and repressors (E2F4-8) competing for similar binding motifs [30-34]. E2F8 target gene repression has been reported critical to induce S-phase arrest in response to DNA damage, allowing DNA repair and maintenance of genetic stability [64, 65]. De-repression of E2F8 targets consequent to *ARID1A*-deficiency could thus lead to an inability to induce s-phase arrest, causing the elimination of tumor cells with replication stress. In turn, the elimination of tumor cells accumulating DNA-damage during cell division aligns with the low number of structural variants and copy number aberrations we observed for *ARID1A* deficient patient tumors (Figure 1, Supplemental Figure 1), and susceptibility of *ARID1A*-deficient tumoroids towards cell cycle checkpoint inhibition (Figure 5).

Similar to the ARID1A-depleted urothelium organoid model, patient-derived tumoroids lacking ARID1A expression and *ARID1A*-deficient MIBC patient tumors also exhibited increased expression of cell cycle checkpoint and DNA repair genes. Prior studies in various malignancies, including BC, have associated *ARID1A* deficiency with impaired DNA double-strand break repair [29, 66, 67] and cell cycle defects [24, 68, 69]. We showed that cell cycle checkpoint inhibition with prexasertib (targeting CHEK1 kinase activity), and YM155 (targeting *BIRC5* transcription) activated apoptotic pathways and cell death in ARID1A-deficient, but not ARID1A-expressing tumoroids. Similar observations have been made recently in a study

by Lo et al., identifying *BIRC5* as a therapeutic target in *ARID1A*-deficient gastric cancer tumoroids[12]. Both prexasertib and YM155 are currently under clinical investigation. Prexasertib monotherapy demonstrated a mild toxicity profile and durable responses in patients with platinum-relapsed ovarian cancer[70], which, like BC, is characterized by frequent somatic *ARID1A* mutations. Notably, prexasertib was granted FDA fast-track designation for treatment of ovarian cancer patients[43]. Meanwhile, YM155 is investigated in a phase II study enrolling B cell lymphoma patients (NCT05263583). Prior phase I/II studies already concluded that YM155 is well tolerated; however, it lacked clinical efficacy in unselected prostate cancer and B cell non-hodgkin lymphoma patients (29-30). Our *ex vivo* response data, however, suggests that YM155 and prexasertib may be more efficacious in patients with *ARID1A*-deficient tumors. Our demonstration that it is feasible to stratify patients by ARID1A IHC, along with favourable toxicity profiles of YM155 and prexasertib, raises the prospect of rapid translation into clinical trials.

In conclusion, our study of ARID1A-depleted human bladder organoids and ARID1A-deficient BC tumoroids enabled the identification of cellular processes disrupted in the context of *ARID1A* deficiency, highlighting the power of this patient-representative platform in disease modelling. Our analyses provide mechanistic insights into secondary dependencies of ARID1A-deficient BC, and our *ex vivo* validation of top therapeutic candidates employing clinically advanced pharmacological inhibitors holds potential for rapid translation into the clinic. Similar strategies employing oncogene-engineered organoids could be extended to encompass a wider range of cancer-associated genes and various types of tumors, potentially yielding valuable clinically relevant insights into oncogenic transformation and, in the end, therapeutic strategies.

METHODS

Organoid/tumoroid culture

Human bladder tissue was obtained from the Erasmus MC Bladder Cancer Center, Rotterdam, the Netherlands, the Amphia Ziekenhuis, Breda, the Netherlands, and the HagaZiekenhuis, The Hague, the Netherlands. Bladder organoids and BC tumoroids from biopsies obtained through TURBT or cystectomy were isolated and cultured using methods developed by Mullenders et al. [20] with modifications. Briefly, bladder tissues were washed with Advanced DMEM/F12 (Gibco) supplemented with 10mM HEPES (Gibco), 1% GlutaMax (Gibco) and 100 µg/ml primocin (InvivoGen), henceforth Ad+++. Tissue was minced and incubated at 37°C with collagenase 2.5mg/ml in EBSS (Gibco) for 60-90 minutes and isolated cells were passed through 70µM strainer (Falcon), washed with Ad+++ and seeded in 50 µl drops of BME (R&D system) containing 10000-15000 cells in 24 well suspension plates (Greiner). Tumoroids and organoids were cultured in a culture medium containing Ad+++ supplemented with 1 × B-27 (Gibco), 1.25 mM N-acetylcysteine (Sigma), 10 mM nicotinamide, 20µM TGFβ receptor inhibitor A83-01, 100ng/ml recombinant human FGF10 (Peprotech), 25 ng/ml recombinant human FGF7 (Peprotech), 12.5 ng/ml recombinant human FGF2 (Peprotech), 10µM Y27632 Rho Kinase (ROCK) Inhibitor (Sigma) and conditioned media for recombinant Rspondin (2.5% v/v), and Wnt3A (2.5% v/v), henceforth bladder organoid medium (BOM). Cultures were passaged at a 1:3 to 1:6 ratio every 7-14 days. For passaging, BME was first digested with 500µg/ml dispase (Gibco, 17105041) for 1 h at 37°C. Cultures were collected in 15mL tubes, Ad+++ was added to 10mL total volume, and organoids were pelleted by centrifugation at 200 x g. Supernatent was discarded, and tumoroids/organoids

were dissociated to single cells using cell dissociation solution-non enzymatic (Sigma, C5914) and mechanical dissociation with a P200 pipette. Dissociated single cells were washed once with 10mL Ad+++, centrifugated at 200 x g, and resuspended in a mixture of culture medium and BME in a 1:2 ratio, and dispersed in new drops. Drops were solidified in the incubator at 37°C for 45 minutes, followed by addition of pre-warmed BOM. Medium was changed every three to four days.

Production of shRNA lentiviral vectors

Lentiviral constructs containing the desired shRNA sequences (shControl - SHC002 and sh*ARID1A* - TRCN0000059089; targeting sequence: GCCTGATCTATCTGGTTCAAT) were amplified from bacterial glycerol stocks obtained in house from the Erasmus Center for Biomics and part of the MISSION® shRNA library. 5.0 x 10^6 HEK293T cells were plated in a 10 cm dish and transfected with 12.5 µg of plasmids mix. 4.5µg of pCMVΔR8.9 (envelope) [71], 2 µg of pCMV-VSV-G (packaging) [71] and 6 µg of shRNA vector were mixed in 500 µL serum-free DMEM and combined with 500 µL DMEM containing 125 µL of 10 mM polyethyleneimine (PEI, Sigma). The resulting 1 mL mixture was added to HEK293T cells after 15 min incubation at room temperature. The transfection medium was removed after 12 hours and replaced with a fresh RPMI medium. Virus-containing medium was harvested and replaced with fresh medium at 48, and 72 hours post-transfection. After each harvest, the collected medium was filtered through a cellulose acetate membrane (0.45 µm pore), concentrated by ultra-centrifugation and used directly for shRNA transductions.

Organoid transduction

Organoids were dissociated to single cell applying the same methods as for passaging. Per condition, 500.000 single cells and 1mL concentrated virus were gently mixed and dispersed into two wells of a 24-well plate. Plates were then centrifuged at 600 x g for 1 hour at 32 °C (spinocculation). The organoid/lentivirus was gently mixed using a P1000 pipette, to detach any adherend cells. Plates were incubated for 5 hours at 37°C, after which single cells were collected in falcon tubes, washed with 10mL ad+++ and centrifuged at 250g for 10 min at 4 °C. Supernatant was removed and transduced cells were seeded in pre-warmed suspension plates. Selection started three days after transduction, using 2 µg/ml puromycin (Invivogen, ant-pr). Puromycin was removed after four days and organoids were cultured for 7-10 days until recovery. Knock-down confirmation was performed with RT-qPCR.

RNA extraction, cDNA synthesis and Real Time-quantitative PCR (RT-qPCR)

Bladder organoids and tumoroids were harvested with dispase, washed once with 10mL Ad+++ and centrifuged for 200 x g for 5 minutes. Then, 1 mL of cold TRIzol (TRI Reagent®, Sigma-Aldrich, T9424) was added to the organoid pellet and the pellet was thoroughly mixed by intermittent vortexing for 1 minute. Samples placed on ice for 10 minutes, prior to storing at -80 C until further processing. RNA was isolated using standard phenol-chloroform RNA extraction. Briefly, frozen samples were equilibrated to room temperature for 15 minutes. Then, 200 µl Phenol:Chloroform:Isoamyl Alcohol 25:24:1 (Sigma-Aldrich, P3803) was added and the samples were thoroughly vortexed and incubated at RT for 2 minutes. Samples were subsequently centrifuged at 12000 x g for 15 min at 4 °C. The aqueous phase was transferred to a fresh Eppendorf tube,

545 500 µl isopropanol (Biosolve Chimie, 220703) was added and samples were incubated for 15 min
546 at RT. Samples were centrifuged (12000 x g, 4 °C, 10 minutes), supernatant was removed and
547 pellets were washed twice with 1 ml 75% ethanol (Honeywell, 32221), centrifuging at 7500 x g
548 for 5 min at 4 °C. As much supernatant was removed as possible, and RNA pellets were air-dried
549 for 20 min at RT. The RNA was dissolved in 20-40 µl nuclease-free water (Promega, P119E),
550 quantified using NanoDrop® Spectrophotometer ND-1000 (Isogen Life Science) and stored at -80
551 °C until further usage.

552 cDNA was synthesized from 500-1000 ng RNA using SuperScript™ II Reverse Transcriptase (200
553 U/µl, Invitrogen, 100004925) according to manufactorers protocol. cDNA samples were diluted
554 to a final concentration of 2.5 ng/µl using nuclease-free water and stored at -20 °C until further
555 usage.

556 RT-qPCR was performed using GoTaq® qPCR Master Mix (Promega, A6002), according to
557 manufacturer's protocols, using CFX96™ Real-Time PCR Detection System (Bio-Rad Laboratories,
558 Singapore). PCR experiments included an initial denaturation at 95 °C for 5 min, 40 amplification
559 cycles starting at 95 °C for 10 sec, followed by 60 °C for 30 sec. Melting curves were assessed by
560 complete annealing and gradual increase in temperature from 65 °C to 95 °C. The data were
561 analyzed using 2-ΔΔCt methods [41], expressed as relative gene expression and normalized to
562 the reference gene Cyclophilin A. Negative controls were used in each reaction plate. The
563 following forward and reverse primers used for RT-qPCR were synthesized by Integrated DNA
564 Technologies: Cyclophilin A (forward: TCATCTGCACTGCCAAGACTG; reverse:

565 CATGCCTTCTTTCACTTTGCC), *ARID1A* (forward: GTCTCAGCAGTCCCAGCAAA; reverse: GATA-
566 GATCAGGCAAGCTGGAGG).

567

568 **Organoid RNA-seq**

569 Total RNA was isolated and quantified as described above. Quality was assessed on a Bioanalyzer
570 (Agilent Technologies) using the Agilent RNA 6000 Nano Kit reagents. Library preparation was
571 performed using the 3' mRNA-seq Library Prep Kit for Ion Torrent (QuantSeq-LEXOGEN, Vienna,
572 Austria). The libraries were quantified and pooled together at a final concentration of 100 pM.
573 The libraries were templated and enriched on an Ion Proton One Touch system and templating
574 was performed using Ion PI Hi-Q OT2 200 Kit (ThermoFisher). The sequencing was performed
575 using Ion PI Hi-Q Sequencing 200 Kit on Ion proton PI V2 chips (ThermoFisher). Fastq files were
576 mapped to the Genome Reference Consortium Human Build 37 (GRCh37), using a two-step
577 alignment process. Firstly, reads were mapped with hisat2 [72], using default parameters. Next,
578 the unmapped reads were mapped with bowtie2 [73] using the --local and --very-sensitive
579 parameters. Counting of the reads on the 3' UTRs was performed with metaseqR2 [74].

580 Differential expression analysis between the tumoroids and organoids was performed with
581 metaseqR2 using the DESEQ2[75] algorithm with default settings and exonFilters = NULL.
582 Expression was corrected for samples derived from the same donor. Pathway enrichment
583 analysis was performed with ReactomePA v1.44.0 [76] using differentially expressed genes with
584 adjusted $p < 0.05$ and log2 fold change > 0.5. Significantly enriched pathways were defined as
585 having adjusted $p < 0.05$ and only the top 5 up- and down- regulated pathways were displayed in

586 the figures. For unsupervised hierarchical clustering, transcript counts were normalized with
587 DESeq2 applying variance stabilizing transformation on protein-coding transcripts. The
588 normalized counts were subsequently median-centered and the Euclidean distance calculated to
589 perform hierarchical clustering with the Ward method. Gene expression signature scores were
590 calculated as the average median-centered expression of genes associated with each signature
591 [7]. Accordingly, for the ARID1A KD comparisons, we employed the PANDORA algorithm within
592 the metaseqR2 package by integrating the DESEQ, DESEQ2, edgeR, limma, NBPSeq, and NOISeq
593 algorithms. Differentially expressed genes were identified based on a meta p-value threshold of
594 < 0.05 and a log2 fold change > 1.

595

596 **The Cancer Genome Atlas (TCGA) bladder cancer cohort**

597 The TCGA data for the bladder cancer cohort is publicly available at
598 https://portal.gdc.cancer.gov./. Somatic mutations detected by Mutect of 412 tumors, GISTIC
599 copy number changes at gene level of 410 tumors, ARID1A protein expression quantified by
600 reverse phase protein array of 127 patients and RNA-seq (HTSeq counts; Affymetrix SNP6 arrays)
601 data available for 410 tumors were analyzed. *ARID1A* was considered deleted when gistic score
602 was <-0.4. Transcript counts were normalized with DESeq2 v.1.32.0 applying variance stabilizing
603 transformation on protein-coding transcripts. Samples were stratified in tertiles according to the
604 ARID1A protein expression into n=42 low, n=43 medium and n=42 high expressed groups. For
605 downstream analysis, samples with protein-coding mutations were excluded, resulting in n=28
606 low, n=29 medium and n=34 high ARID1A expressed groups. RNA counts were used for

607 differential gene expression analysis between *ARID1A* deleted samples vs the rest, low ARID1A
608 protein-expressed samples vs the rest and low *ARID1A* mRNA-expressed group vs the rest.
609 Differentially expressed genes had adjusted $p < 0.05$ and absolute log2 fold change > 1.
610 Multivariate cox regression analysis was applied using the survival R package[77].

611

612 **HMF metastatic urothelial cancer cohort**

613 WGS and RNA-seq data from metastatic urothelial carcinomas are available through the
614 Hartwig Medical Foundation at https://www.hartwigmedicalfoundation.nl/en/data/data-
615 access-request/, under request number DR-314. Samples that were previously analyzed by
616 Nakauma-Gonzalez et al.[7] were retrieved from DR-314 and re-analyzed with the same
617 bioinformatics pipeline using the human reference genome hg19. *ARID1A* was considered
618 deleted when gistic score was <-0.9. RNA counts were normalized with DESeq2 v.1.32.0
619 applying variance stabilizing transformation on protein-coding transcripts.

620 **Histology & Histochemistry**

621 Patient tissue was processed using standard procedures. For tumoroid and organoid processing,
622 tumoroids/organoids were fixed within BME-drops using 4% paraformaldehyde + 0.2%
623 glutaraldehyde (in-house produced) at room temperature for two hours. Fixed BME-drops were
624 then pre-embedded in 4% agarose prior to paraffin embedding. H&E staining were done
625 automatically in the HE600 (Ventana). Alcian Blue staining was done automatically according to
626 the manufactures instructions on the Ventana special stains (#860-002, Ventana).

Immunohistochemistry

Protein expression of UCC differentiation markers and ARID1A was investigated by automated IHC using the Ventana Benchmark ULTRA (Ventana Medical Systems Inc.). Sequential 4 µm thick (FFPE) sections were stained for markers indicated below (Table 1) using Optiview detection (OV) (#760-700, Ventana) or Ultraview detection (UV) (#760-500, Ventana). In brief, following deparaffinization and heat-induced antigen retrieval with CC1 (#950-500, Ventana), the tissue samples were incubated with antibody of interest for the indicated time (Table 1). Incubation was followed OV, UV detection and hematoxylin II counter stained for 8 minutes followed by a blue coloring reagent for 8 minutes according to the manufactures instructions (Ventana).

Table 1. Immunohistochemistry information

Antibody	**Dilution**	**Species**	**Company**	**Catalog and Clone**	**Pretreatment in minutes**	**Ab incubation time** at 37˚**C**
GATA3	1,63 µg/ml	Mouse	Cell Marque	L50823	CC1 32’ OV	48 minutes
KRT5	0,21 µg/ml	Rabbit	Cell Marque	SP27	CC1 64’ UV	32 minutes
ARID1A	1/1000	Rabbit	Abcam	EPR13501	CC1 32’ OV	32 minutes
KRT20	0,16 µg/ml	Rabbit	Ventana	SP33	CC1 32’ OV	24 minutes
Synaptophysin	0,06 µg/ml	Rabbit	Ventana	SP11	CC1 32’OV	24 minutes

SNaPshot mutation analysis

DNA was isolated using with the QIAmp DNA Mini-Kit (Qiagen) according to the manufacturer’s protocol. Presence of hotspot mutations in the *TERT* promoter sequence chr5:1,295,228C>T, chr5:1,295,248G>A and chr5:1,295,250C>T [GRCh37/hg19]), *FGFR3* (R248Q/E, S249C, G372C, Y375C, A393E, K652E/M) and *PIK3CA* (E542K, E545G/K and H1047R) were assessed on tumor, tumoroid, normal adjacent urothelium and organoid DNA by SNaPshot mutation analysis with the same methods as previously described [25-27]).

Copy-number aberration analysis in tumoroid/organoid samples

Copy number aberration analysis was performed using single-nucleotide polymorphism (SNP) microarrays (Infinium Global Screening Array (GSA) V3, Illumina) on tumor, tumoroid, normal adjacent urothelium and organoid DNA using standard protocols. SNP data (log-R ratio, B-allele frequency) were visualized to identify potential CNVs via Biodiscovery Nexus CN7.5. (Biodiscovery) and the GenomeStudio genotyping module (Illumina).

Immunofluorescence

Bladder cancer tumoroids/organoids were cultured and stained in chamber slides (ThermoFisher, 154526PK) prior to fixation with 4% paraformaldehyde for 20 minutes at room temperature. Organoids were washed three times with PBS followed by a 30 minute treatment with 0,1M glycine and 30 minute permeabilization with 0.5% Triton X-100 (Sigma) in PBS, both at room temperature. Organoids were blocked with 0.3% Triton-X-100 (Fluka, 93426), 1% DMSO (Honeywell Riedel-de Haën, 34869), and 0.5% goat serum (Vector Laboratories, S 1000), in PBS at room temperature for 2 hours. Following blocking, organoids were incubated overnight with primary antibodies: KRT5 (Bio Legend; 905901), KRT20 (Dako; M7019), GATA3 (Cell Signaling Technology, D13C9). After three washes in PBS, organoids were stained with appropriate Alexa Fluor dye-conjugated secondary antibodies (Invitrogen), 1:1000 for 1 hour at room temperature. Chambers were removed from the slides and slides were mounted with DAPI (Southern Biotech, 0100-20) and a cover slide. Immunofluorescence images were acquired using a confocal microscope (Leica, Stellaris). Brightness and contrast was adjusted in Image J.

666

667 ***Ex vivo* drug response**

668 Bladder tumoroids were cultured for 7-10 days in BME prior to harvesting and dissociation to
669 single cells as previously described. Per condition, 10.000 cells were seeded in 100µl bladder
670 organoid medium containing 15% BME. YM-155 (PBS, Selleckchem, S1130) and prexasertib
671 (DMSO, Selleckchem, LY2606368) were added when mature organoids formed after two-three
672 days, and drug treatment was performed in triplicate. Tumoroids were treated with
673 concentrations as indicated, and treatment lasted four days (96h) prior to viability assessment,
674 whereas a two day (48h) treatment was used for other read-outs. Concentrations used for single-
675 dose treatment (prexasertib 32nM and YM155 50nM) were based on average IC50 values of
676 ARID1A-expressing and ARID1A-deficient tumoroid lines. Following treatment, cell viability was
677 assessed by by cellTiter-Glo 3D (Promega, G9681) and Caspase 3/7 activity by Caspase-Glo
678 (#G8093, Promega). Plates were read on a SpectraMax I3 plate reader. Viability data was
679 normalized using organoid wells treated with vehicle control (0.02% DMSO, 1.2% PBS). Presented
680 data are triplicates from two independent experiments.

681 For fluorescence analysis of caspase 3/7 activity, treated organoids were harvested with dispase,
682 and washed 2 times with Ad+++ to completely remove BME. Organoids were processed in a 96
683 well flat, clear-bottom microscopy plate (Revvity, 6005225). Organoids where incubated with
684 caspase 3/7 activity dye (CellEvent™ Caspase-3/7 Detection Reagents, 1:1000 in BOM) for 30
685 minutes at 37°C, followed by fixation with 4% paraformaldehyde at room temperature for 30
686 minutes. Organoids were washed once with 200µL PBS, followed by staining with 2 µg/mL

687 Hoechst33342 (Molecular Probes) in 200 µL PBS at 4°C for 12 hours. Plate was imaged with the
688 Opera Phenix Plus High-Content Screening System (Revvity, Waltham, MA, USA). Pre-scanning
689 using 10x bright field images was performed to identify fields of view containing organoids. Fields
690 of view containing organoids were then imaged at 40X magnification for confocal and 20x for
691 bright field, covering the center of each well. 25 Fields of view were imaged per condition.
692 Image analysis was performed with the Harmony software (Revvity). Hoechst was imaged
693 excitation 405nm, emission 435-480nm, caspase reporter activity with excitation 488nm,
694 emission 500-550nm. Briefly, organoids containing at least three nuclei were automatically
695 segmented and mean caspase reporter intensity per organoids was calculated for all conditions.
696 Measurements were obtained for at least 49 organoids per condition and statistical analysis was
697 performed using a mixed-effect analysis due to different samples sizes. For image display, raw
698 images were exported and brightness and contrast was adjusted in imageJ.

699 For fluorescent Live/Dead staining, treated tumoroids were harvested using dispase and washed
700 once with 500µl PBS. Tumoroids were stained with fixable live/dead staining
701 (Invitrogen™L34975) 1:500 in PBS for 15 minutes PBS, following reconstitution according to
702 manufacturer's protocol (Invitrogen, L34994). Tumoroids were quenched with 1mL PBS + 5% FCS
703 and fixated with 4% paraformaldehyde at room temperature for 30 minutes. Organoids were
704 washed once with 500µL PBS, followed by staining with 2 µg/mL Hoechst33342 (Molecular
705 Probes) in 200 µL PBS at 4°C for 12 hours. Tumoroids were transferred to a 96 well flat, clear-
706 bottom microscopy plate (Revvity, 6005225), and the plate was imaged with the Opera Phenix
707 Plus High-Content Screening System (Revvity). Pre-scanning using 10x bright field images was
708 performed to identify fields of view containing organoids. Fields of view containing organoids

were then imaged at 40X magnification for confocal and 20x for bright field, covering the center of each well. 25 Fields of view were images per condition. Hoechst was imaged excitation 405nm, emission 435-480nm, fixable live/dead staining with excitation 488nm, emission 500-550nm. Image analysis was performed with the Harmony software (Revvity). Software was set to measure mean signal intensity of live/dead dye in the inner 60% of the tumoroids, excluding the outer rim in order to limit detection of non-specific staining on the outside of the organoids. For image display, raw images were exported and brightness and contrast was adjusted in imageJ unless stated otherwise.

Flowcytometry

For flow cytometry, tumoroids were treated with 32 nM prexasertib, 50 nM YM-155, or vehicle control for 48 hours. Tumoroids were harvested with dispase, and dissociated with non-enzymatic dissociation solution. Single cells were washed twice and stained with fixable live/dead staining (Invitrogen™L34975) 1:1000 in PBS for 15 minutes, followed by one wash with PBS + 5% FCS, and fixation in 100% methanol for 20 minutes. Samples were stored at 4°C for up to a week or stained fresh. Antibody staining was performed on ice for 3 hours with mouse anti-γH2AX (4ug/mL) CAT#) in permeabilization and blocking buffer, followed by two washes in permeabilization and blocking buffer. Subsequent secondary staining was done with anti-mouse Alexa 647 (4ug/mL CAT#) for 90 minutes on ice, followed by two washes with permeabilization and blocking buffer. Cells were subsequently stained with 50 µg/mL propidium iodide (PI) (Sigma) and 0.2 mg/mL RNAse A (10109142001, Sigma-Aldrich) for 30 minutes at room temperature. Stained cells were then FACS-analyzed using a 655 LP and a 695/40 BP filter. Events were gated for single, and live cells based on PI intensity and live/dead staining. Tumoroid-specific gates were

731 set to determine the fraction of γH2AX positive cells and cell cycle distribution. Prexasertib and
732 YM155 treatment distorted cell cycle distribution in such extend that a clear distinction between
733 phases S and G2/M was not possible, requiring the merging of S, G2 and M in further analyses.
734 One-way ANOVA was used to compare γH2AX positive fractions and cell cycle distribution
735 between ARID1A-expressing and ARID1A-deficient tumoroids.

736

737 **Statistical Analysis**

738 All data from lab experiments are presented as mean ± standard error of the mean (SEM) and
739 are the result of two independent experiments performed in triplicate, unless stated otherwise.
740 Statistical significance was calculated as indicated in figure legends. GraphPad Prism for Windows
741 (version 9.0.0, GraphPad Software, La Jolla, CA, USA) was used for statistical analysis of wet lab
742 experiments. For genomics and transcriptomics data analyses, the Wilcoxon-rank sum test was
743 used for comparison of 2 groups with continuous variables. The log-rank tests were used for
744 comparing overall survival displayed as Kaplan–Meier survival curves. Differential expression
745 analysis of transcripts was performed using the Wald test with DESeq2 v1.32.0 [75]. A gene list
746 of differentially expressed genes was supplied to ReactomePA v1.44.0 [76] to identify enriched
747 pathways with *p* values estimated by hypergeometric distribution. *p* values were adjusted for
748 multiple testing using the Benjamini–Hochberg method and are indicated as adjusted *p* values.
749 Genomics and transcriptomics data analyses were performed using the platform R v4.3.2 [78].

750 **Data Availability**

751 All data needed to evaluate the conclusions in the paper are present in the paper and/or the
752 Supplementary Materials. All RNA-seq data generated in this study have been deposited to the
753 Gene Expression Omnibus (GEO) database with accession code X. WGS and RNA-seq data from
754 metastatic bladder cancers were requested via the Hartwig Medical Foundation at
755 https://www.hartwigmedicalfoundation.nl/en/data/data-access-request/, and approved under
756 request number DR-314. The TCGA data for the bladder cancer cohort is publicly available at
757 https://portal.gdc.cancer.gov./. Source data are provided with this paper. Additional data related
758 to this paper may be requested from the authors.

Supplemental material version: 240526

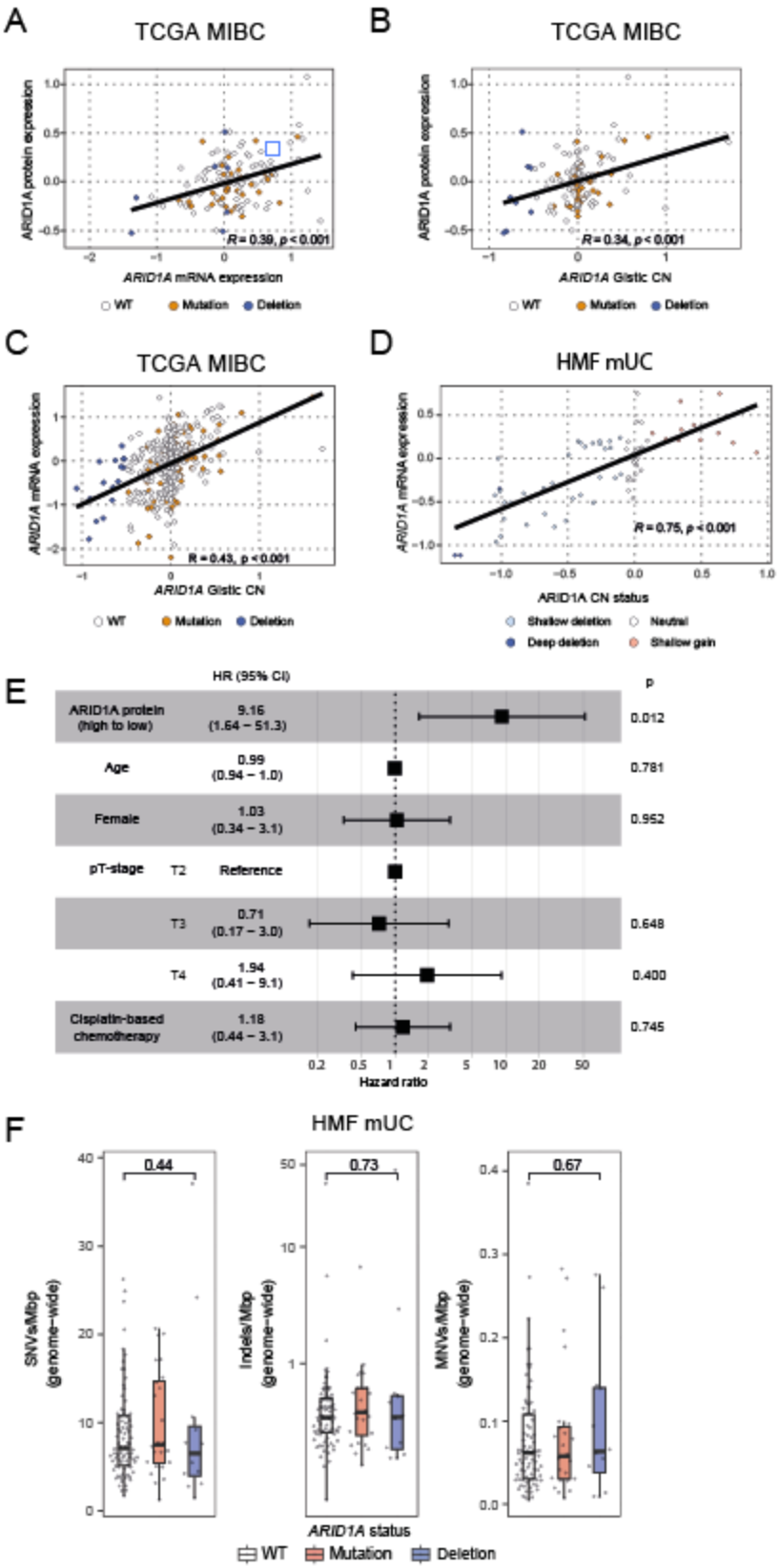

Supplemental Figure 1. Pearson correlation between **A)** ARID1A protein expression levels and *ARID1A*

mRNA expression, **B)** *ARID1A* protein expression and *ARID1A* gistic copy number levels, and between **C)** *ARID1A* mRNA expression and *ARID1A* gistic copy number levels in MIBC tumor samples*. **D)** Pearson correlation between *ARID1A* mRNA expression and *ARID1A* copy number status in mUC samples**. **E)** Overview of hazard ratios (HR) calculated for ARID1A protein expression and clinical features for MIBC patients*. Continuous variables were dichotomized based on the median and high vs. low is presented. Boxes indicate HR and horizontal lines show 95% confidence intervals (CI). **F)** Boxplots depicting the number of single-nucleotide variants (SNVs), insertions and deletions (indels), and multi-nucleotide variants (MNVs) per mega base pairs (MBp) in metastatic BC patients stratified on *ARID1A* mutation status. Two-sided Wilcoxon-rank sum test was applied to compare differences between samples with *ARID1A* WT and *ARID1A* deletions. For all graphs: WT = *ARID1A* wild type, Mutation = protein-coding mutation (excluding synonymous) and small insertions/deletions, Deletion = *ARID1A* deleted. *TCGA **HMF.

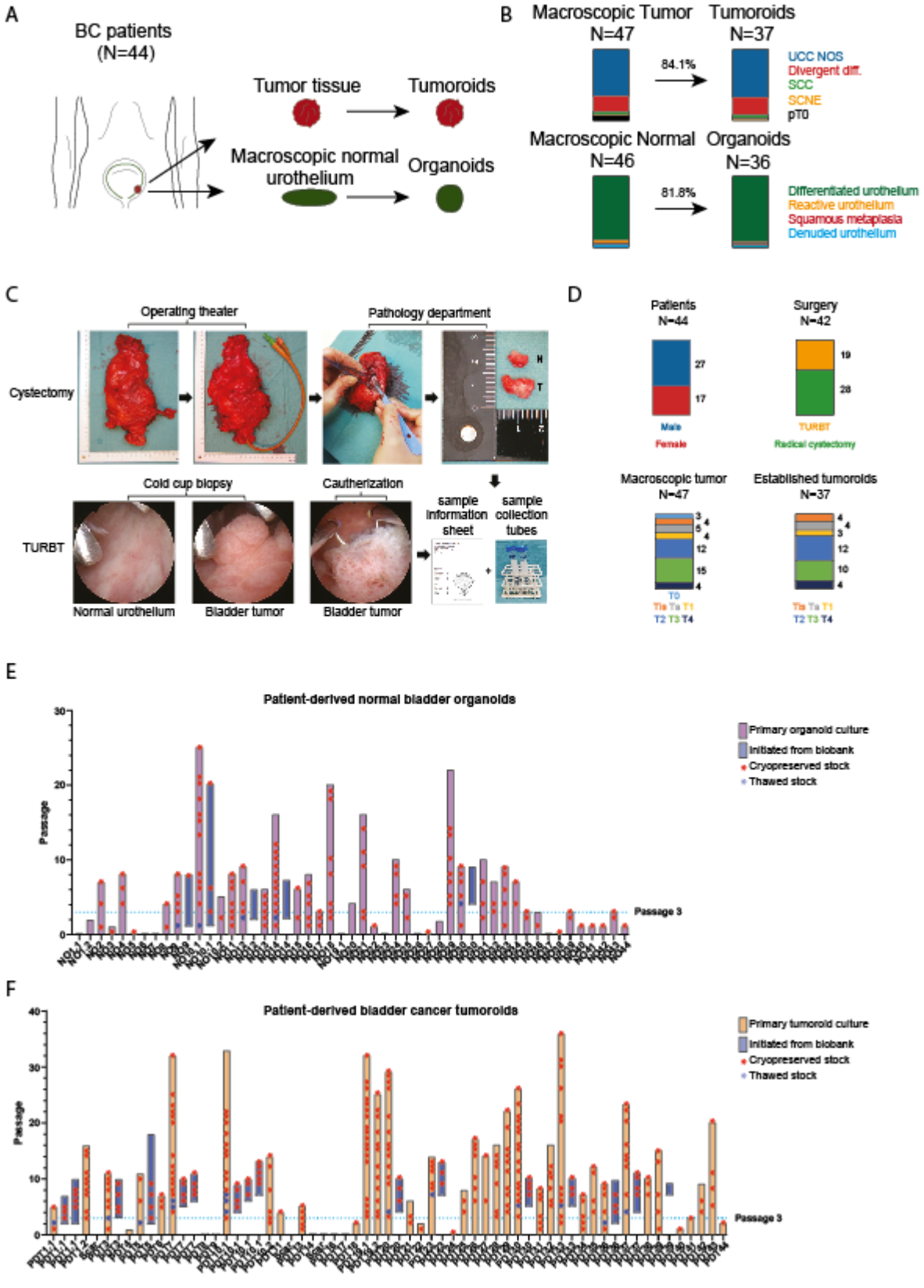

774

Supplemental Figure 2. A) Diagram depicting the generation of patient-derived bladder tumoroids and normal organoids from primary tissues. Tumoroids are generated from tumor tissue, while organoids are generated from macroscopic normal urothelium. **B)** Top: Bar charts comparing the stratification of tumor samples with derived organoid lines based on histological subtype observed in the tumor samples UCC NOS = urothelial carcinoma not otherwise specified, Divergent diff. = divergent differentiation, SCC = squamous cell carcinoma, SCNE = small cell neuroendocrine. Bottom: Bar charts comparing stratification of macroscopic normal urothelium and derived organoid lines based on histological evaluation of macroscopic normal urothelium. **C)** Schematic depiction of sample acquisition. Bladders are instilled with cold preservation fluid immediately following radical cystectomy. Instillation occurs through an indwelling catheter, which is then plugged to prevent leakage during transport to the gross room. Bladders are kept inside an endobag and on ice to maintain sterility and preserve cell viability during transport. At the gross room, bladders are ventrally incised and normal (N) and tumor (T) samples are excised on a sterile field using disposable lancets and tweezers to prevent contamination. For transurethral resection of bladder tumor (TURBT), macroscopic normal urothelial tissue is sampled by cold cup biopsy prior to resection. Bladder tumor samples are thereafter acquired by cold cup biopsy or cautherization when biopsies were not possible due to limited visibility. Acquired samples are stored in collection tubes containing cold preservation fluid and are then transported to the laboratory facilities, along with a sample information sheet containing pseudomized baseline clinical information and study identification. **D)** Bar charts depicting patient characteristics and comparing stratification of all acquired macroscopic tumor tissue with that of all patient-derived tumoroid lines. N=39 patients underwent 42 surgical procedures. Top left: biological sex, top right: type of resection, bottom left: pathological tumor stage of all acquired samples, bottom right: pathological tumor stage corresponding to successfully initiated cultures. The composition of included patients and organoid lines is characteristic for a tertiary referral center and tumoroids were established from BC patients with various tumor stages without bias. **E)** Bar graph summarizing the established normal organoid biobank. Each bar represents one organoid line (purple bars) or derivative initiated from cryopreserved stocks (blue bars). Cryopreserved stocks are indicated by red asterisks, while thawed stocks are indicated by blue asterisks. **F)** Bar graph the established BC tumoroid biobank. Each bar represents one tumoroid line (yellow bars) or derivative initiated from cryopreserved stocks (blue bars). Cryopreserved stocks are indicated by red asterisks, while thawed stocks are indicated by blue asterisks.

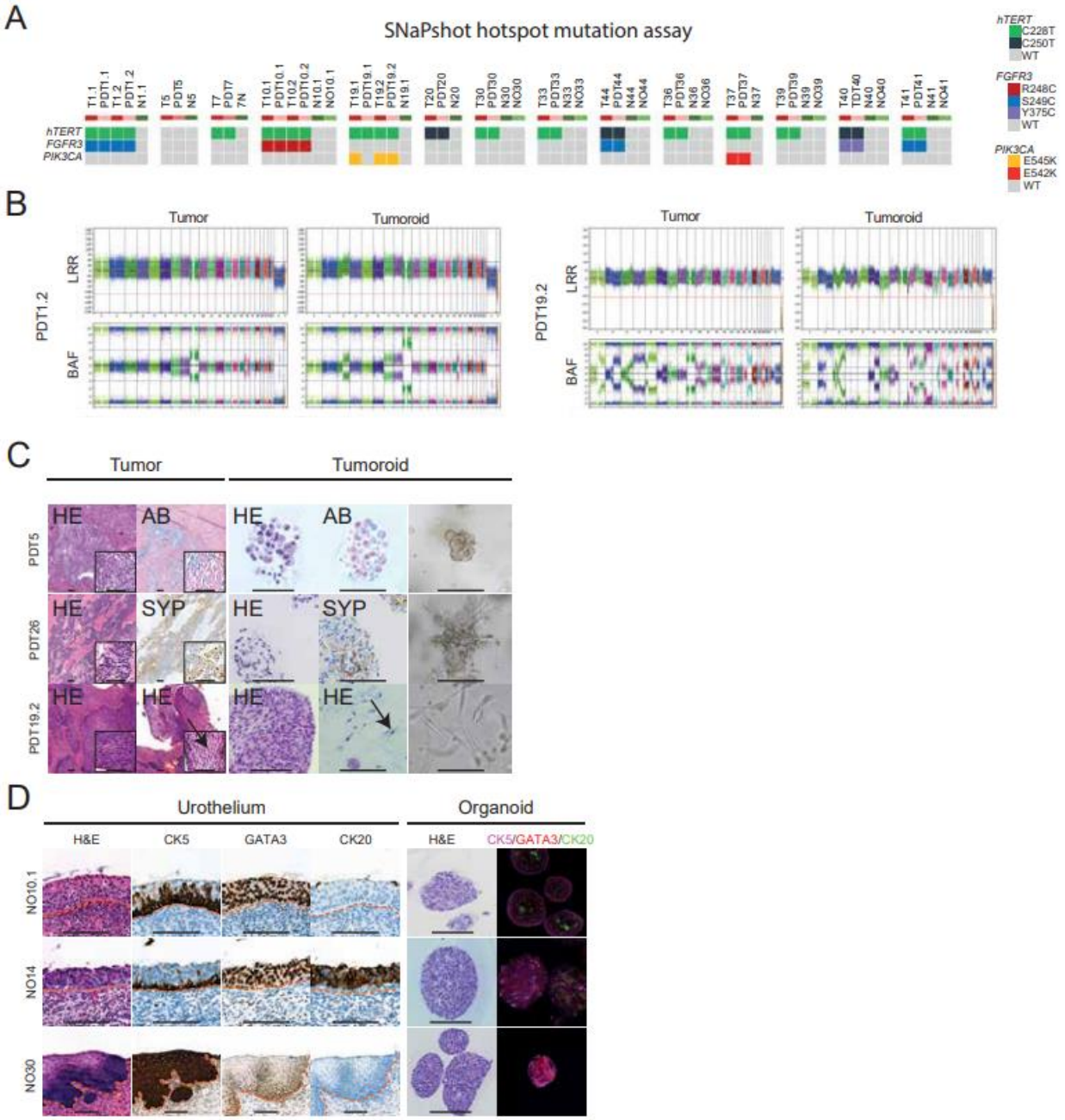

Supplemental Figure 3. A) SNaPshot mutation analysis of patient tumor (T) and normal (N) samples and matched patient-derived tumoroid (PDT) and normal organoid (NO) cultures on recurrent somatic hotspot mutations in telomerase reverse transcriptase (hTERT), fibroblast growth factor receptor 3 (FGFR3), and Phosphatidylinositol-4,5-Bisphosphate 3-Kinase Catalytic Subunit Alpha (PIK3CA) genes, WT = wild type. **B)** Scatterplots illustrating genome wide copy number alterations depicted by Log R ratios (LRR) and B-allele frequency (BAF) from PDT1.2 and PDT19.2 tumor tissue and corresponding tumoroids. Note increased resolution of copy number alterations in tumoroid samples **C)** Comparative histological and

816 immunohistochemical images of variant histology in bladder tumor tissue and corresponding tumoroid
817 lines. Shown are representative examples of choroid differentiation, as well as small cell neuroendocrine
818 and squamous cell carcinoma variant histology. Choroid differentiation (PDT5) shows signs of mucus
819 production indicated by alcian blue (AB) positivity. Small cell neuro-endocrine bladder cancer (PDT26)
820 stained positive for synaptophysin (SYP). Squamous cell carcinoma (PDT19.2) was identified by “tadpole”
821 cells (black arrow) and keratinization. Two columns on the left demonstrate histological and
822 (immune)histochemical images of bladder tumor tissue while the three columns on the right indicate
823 patient-derived tumoroid lines. Scale bar = 50 µm. **D)** Histological evaluation of macroscopic normal
824 bladder tissue and corresponding organoids. Two representative examples of normal urothelium (NO10.1
825 & NO14), in addition to one squamous metaplasia sample (NO31) are shown. Organoids and originating
826 tissue were compared by H&E staining, while expression of urothelial differentiation markers was
827 investigated by IHC (original tissue) and IF (organoids) as indicated. (scale bar = 50 µm).

828

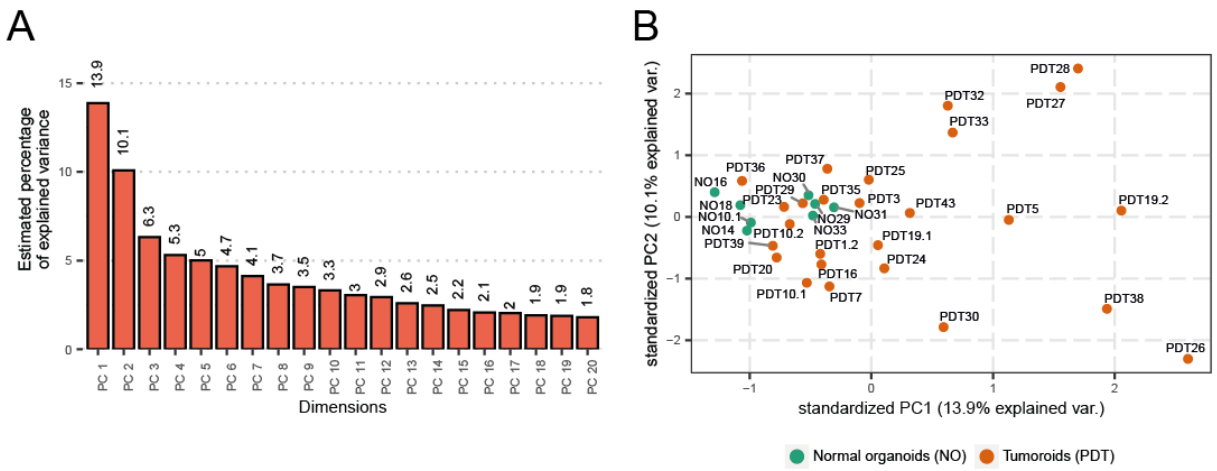

Supplemental Figure 4. A) Bar graph depicting estimated variance in gene-expression by the top 20 principal components. **B)** Distribution of tumoroids and normal bladder organoids within the first two principal components (PCA1-2).

835

A

Homer *de novo* Motif Enrichment

p-value:	1e-18
log p-value:	-4.184e+01
Information Content per bp:	1.592
Number of Target Sequences with motif	55.0
Percentage of Target Sequences with motif	25.50%
Number of Background Sequences with motif	2543.8
Percentage of Background Sequences with motif	5.81%
Average Position of motif in Targets	408.8 +/- 151.1bp
Average Position of motif in Background	348.4 +/- 198.2bp
Strand Bias (log2 ratio + to - strand density)	0.8
Multiplicity (# of sites on seq that occur together)	1.16

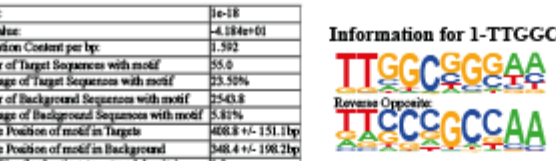

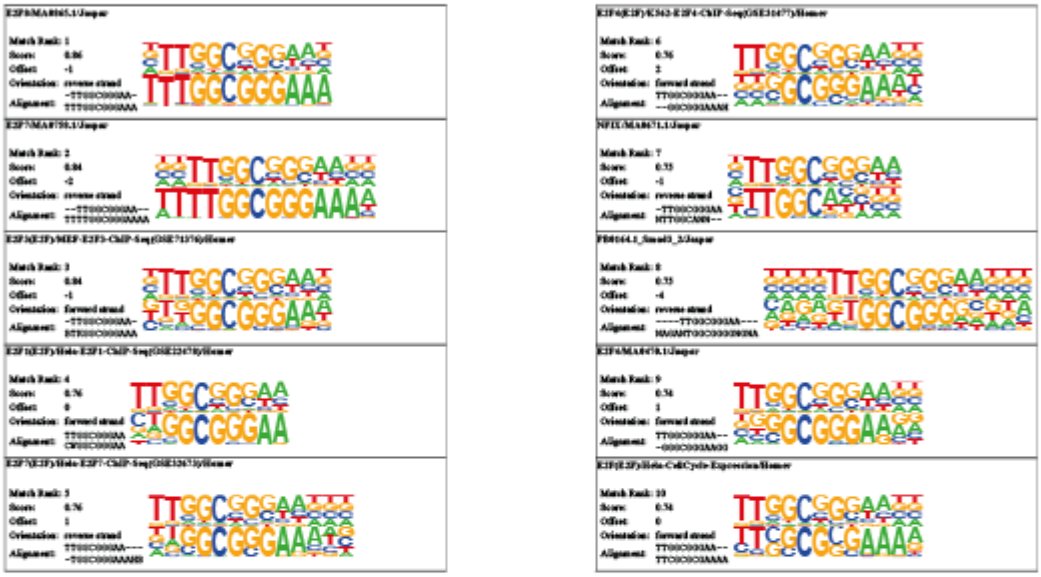

B

E2F8 consensus sequence instances

GeneID	PromoterID	Offset	Sequence	Refseq	Ensembl	up/down-regulated in shARID1A
3833	NM_002263	-296	TTTGGTGAGAAA	ENSG00000237649	KIFC1	up-regulated
4174	NM_006739	24	TTTCCCGCGAAA	ENSG00000100297	MCM5	up-regulated
8318	NM_003504	69	TTTGGCGGGAGT	ENSG00000093009	CDC45	up-regulated
4605	NM_002466	53	CTTGGCGGGAGA	ENSG00000101057	MYBL2	up-regulated
1869	NM_005225	-1	TTTGGCGCGTAA	ENSG00000101412	E2F1	up-regulated
2145	NM_001991	-106	TTTGGCGGCAAA	ENSG00000108799	EZH1	up-regulated
81620	NM_030928	-16	TTTGGCGGGAAC	ENSG00000167513	CDT1	up-regulated
5888	NM_002875	36	TTTGGCGGGAAT	ENSG00000051180	RAD51	up-regulated
9824	NM_014783	-418	GTTCCCACCAAG	ENSG00000198826	ARHGAP11A	up-regulated
91750	NM_001024674	-373	TTAGGAGCGAAA	ENSG00000205659	LIN52	up-regulated
221150	NM_145061	-410	CTTGGCGCGCAA	ENSG00000165480	SKA3	up-regulated
9700	NM_012291	-18	TCTGGCGCGGAA	ENSG00000135476	ESPL1	up-regulated
1111	NM_001274	-400	TTTGGCGGGAAA	ENSG00000149554	CHEK1	up-regulated
374393	NM_198947	-4	CTAGGCGGGAAA	ENSG00000189057	FAM111B	up-regulated
79733	NM_024680	-180	TTCCGCGCCAAA	ENSG00000129173	E2F8	up-regulated
3070	NM_018063	24	TTTCCCGCGAAG	ENSG00000119969	HELLS	up-regulated
79075	NM_024094	88	TTGCCCGCCAAG	ENSG00000136982	DSCC1	up-regulated
2146	NM_004456	-355	GTTCCCGCCAAG	ENSG00000106462	EZH2	up-regulated
231	NM_001628	-205	TTTCCCACCAGA	ENSG00000085662	AKR1B1	up-regulated
7980	NM_006528	80	CTTGGCGGGGAA	ENSG00000105825	TFPI2	up-regulated
64946	NM_022909	-435	TTCTCCGCCAAA	ENSG00000153044	CENPH	up-regulated
4085	NM_002358	43	CTTGGCGGGGAA	ENSG00000164109	MAD2L1	up-regulated
11073	NM_007027	-59	GTTGGCGCGAAA	ENSG00000163781	TOPBP1	up-regulated
4175	NM_005915	-56	TTTGGCGCGAAA	ENSG00000076003	MCM6	up-regulated
2956	NM_000179	77	TTTCCCGCCAGC	ENSG00000116062	MSH6	up-regulated
7923	NM_014234	-182	TTTGGGGGGAAT	ENSG00000204228	HSD17B8	down-regulated
8996	NM_003946	-107	TTAGGTGGGGAA	ENSG00000140939	NOL3	down-regulated
735301	NR_003142	-371	TTTGCTGGGAAA	ENSG00000255198	SNHG9	down-regulated
54997	NM_017899	-294	TTTCCCTCCTAA	ENSG00000088992	TESC	down-regulated
55118	NM_018058	-320	CCTGGGGGGAAA	ENSG00000095713	CRTAC1	down-regulated
259230	NM_147156	-396	CTTGGTGGGAAA	ENSG00000198964	SGMS1	down-regulated
10395	NM_006094	-473	GTTCCCGCCAGG	ENSG00000164741	DLC1	down-regulated

836

837 **Supplemental Figure 5. A)** *De novo* binding motif (Motif 1) and matched known binding sequences as

838 predicted by Homer. **B)** E2F8 consensus sequence instances in dysregulated genes upon ARID1A knock-
839 down in bladder organoids.

840

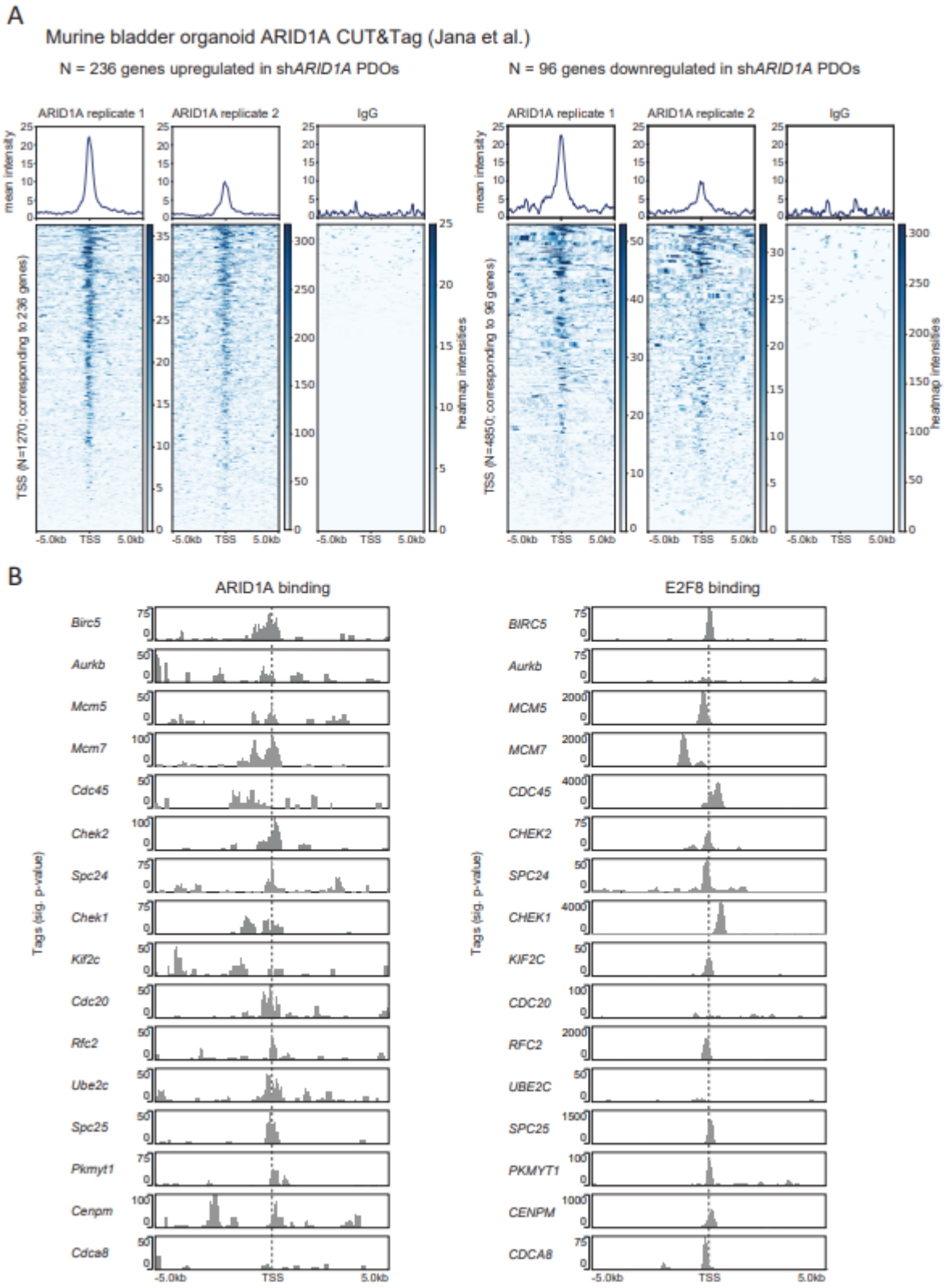

Supplemental Figure 6. A) Histograms (top) and heatmaps (bottom) depicting mean ARID1A binding intensities around 1270 transcription start sites (TSS) corresponding to N = 236 genes upregulated (left)

or N=96 downregulated (right) upon ARID1A knock-down in normal organoids. N= 10 genes did not have a murine orthologue and where excluded from analysis. CUT&Tag analysis was performed in murine urothelial organoid cells with ARID1A-directed antibodies, using IgG as control as indicated. Data was repurposed from Jana et al. **B)** Left: ARID1A occupancy at transcription start sites of 16 candidate genes in murine urothelial organoids. Data was repurposed from Jana et al. (29). Right: E2F8 occupancy at transcription start sites of 16 candidate genes in K562 myeloid progenitor cells. Data was repurposed from the ENCODE project (35).

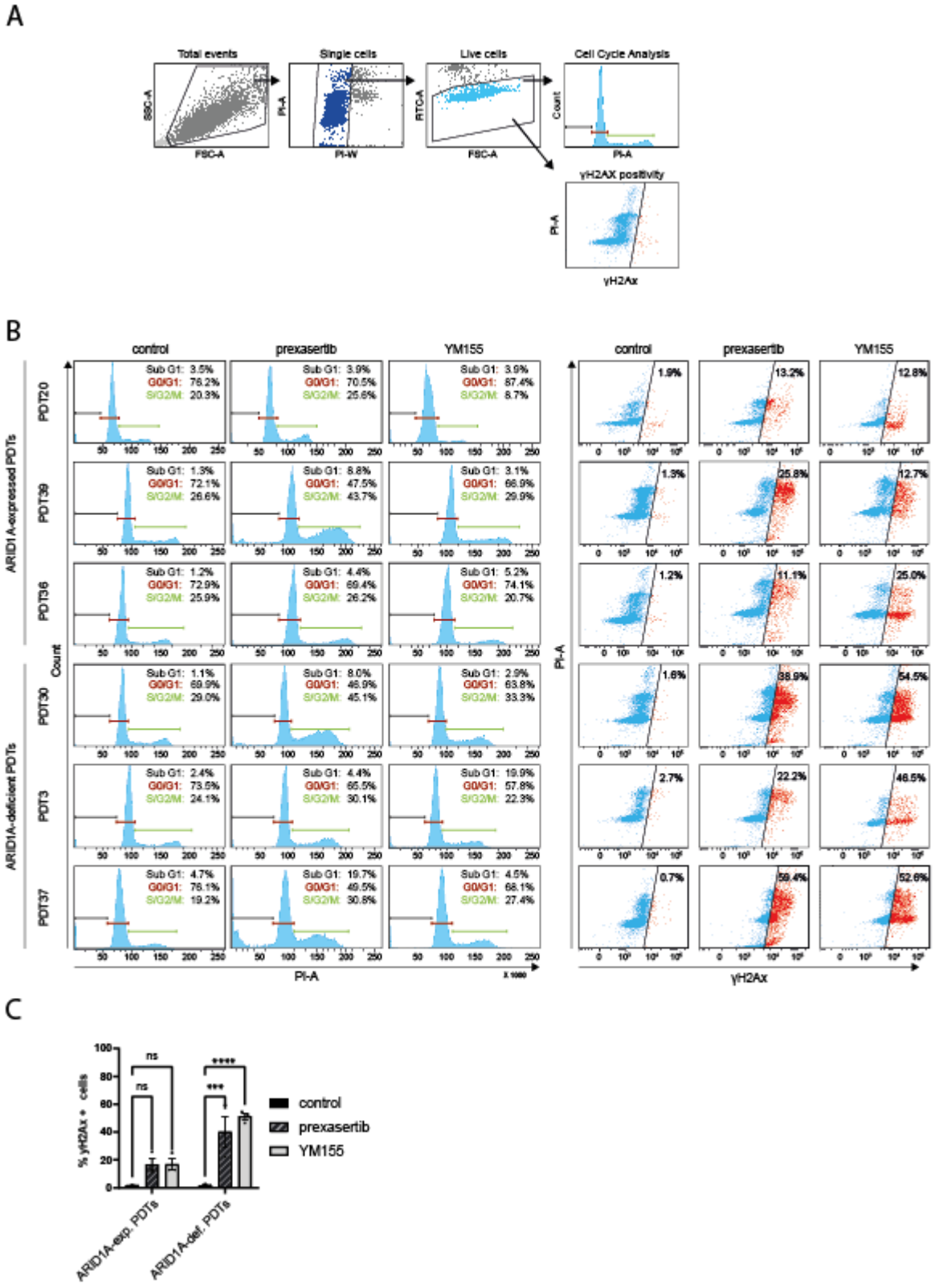

Supplemental Figure 7. A) Sequential gating strategy to identify single cells: initial gating on FSC-A vs SSCA to define the region of interest by excluding very small particles and multicellular aggregates, on

the left, followed by single cells gating in PI-A vs PI-W, cell cycle analysis using a mono-dimensional PI-A histogram in a linear scale, and gating strategy to define the percentage of γH2AX+ cells in the live fraction. **B)** Flow cytometry on ARID1A-expressing tumoroids (PDT20, PDT36, PDT39) and ARID1A-deficient tumoroids (PDT3, PDT30, and PDT37) treated with 32nM prexasertib or 50nM YM155 for two days. Gating on single live cells was followed by cell cycle analysis (left) and measurement of the fraction of cells with phosphorylated H2Ax (γH2Ax) (right). **C)** Bar graph depicting γH2Ax+ fraction of ARID1A-expressing (PDT20, PDT36, PDT39) and ARID1A-deficient (PDT3, PDT30, and PDT37) tumoroids treated with 32nM prexasertib or 50nM YM155 compared to untreated control. Gating on single live cells was followed by measurement of γH2Ax+ positive fraction, as shown in B. Drug treated ARID1A-expressing and ARID1A-deficient tumoroids are compared to the respective untreated controls, however, source data corresponds to that presented in Figure 5C. Data are represented as mean ± SEM.

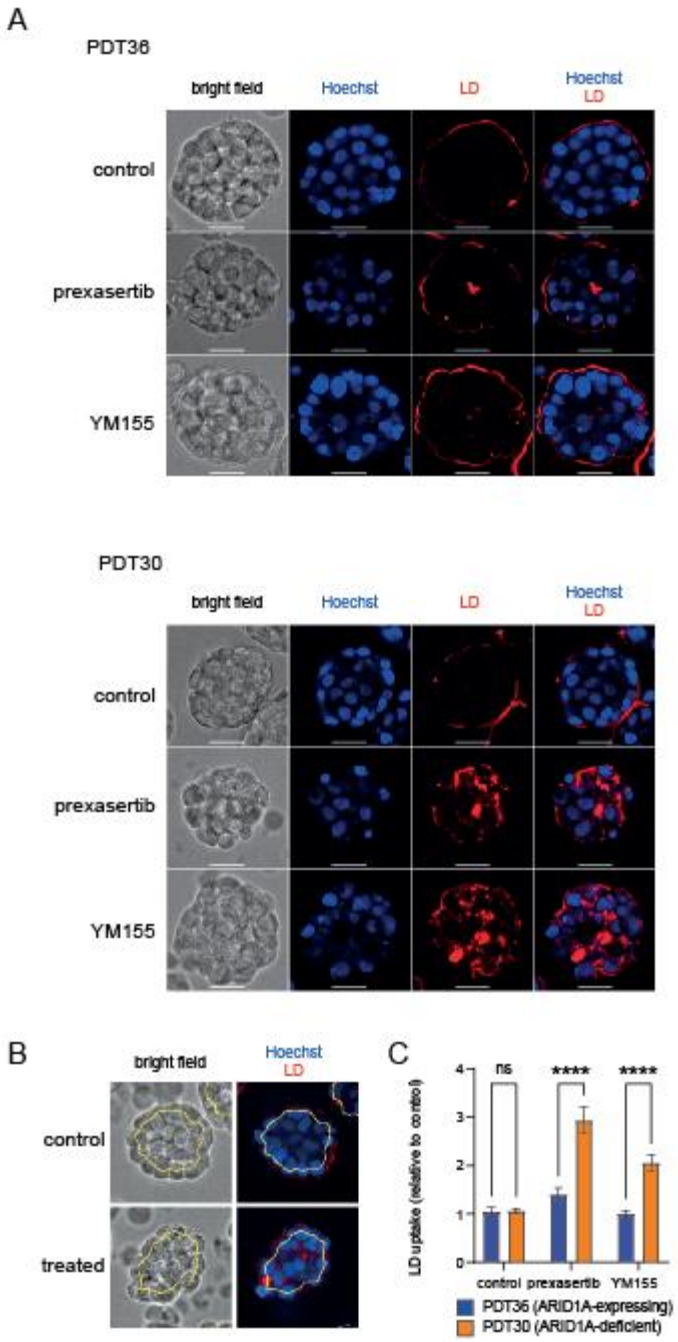

866

867 **Supplemental Figure 8. A)** Representative brightfield and fluorescence staining showing fixable Live/Dead
868 (LD) cell staining (red) in *ARID1A*-expressing (PDT36) and *ARID1A*-deficient (PDT30) bladder tumoroids
869 treated for 48 hours with 32nM prexasertib or 50nM YM155, compared to untreated controls. Hoechst
870 (blue) was used as a counter staining. Raw images were exported from Harmony software and brightness
871 and contrast was adjusted in imageJ **B)** Representative images depicting automated tumoroid
872 segmentation (yellow line) by the Harmony software to select the inner 60% of tumoroid surface area in
873 order to quantify tumoroid uptake of fixable live/dead staining. Processed Images were exported from
874 Harmony software and contain gamma correction as implemented by Harmony software. Segmentation

line was manually accentuated in illustrator **C)** Bar graph depicting mean uptake of fixable LD staining per tumoroid. LD uptake was measured in the inner 60% of tumoroid surface area. At least 100 tumoroids were measured per condition and no gamma correction was applied prior to measurement. Data are presented as mean +-SEM. **P<0.005, ****P<0.00005.

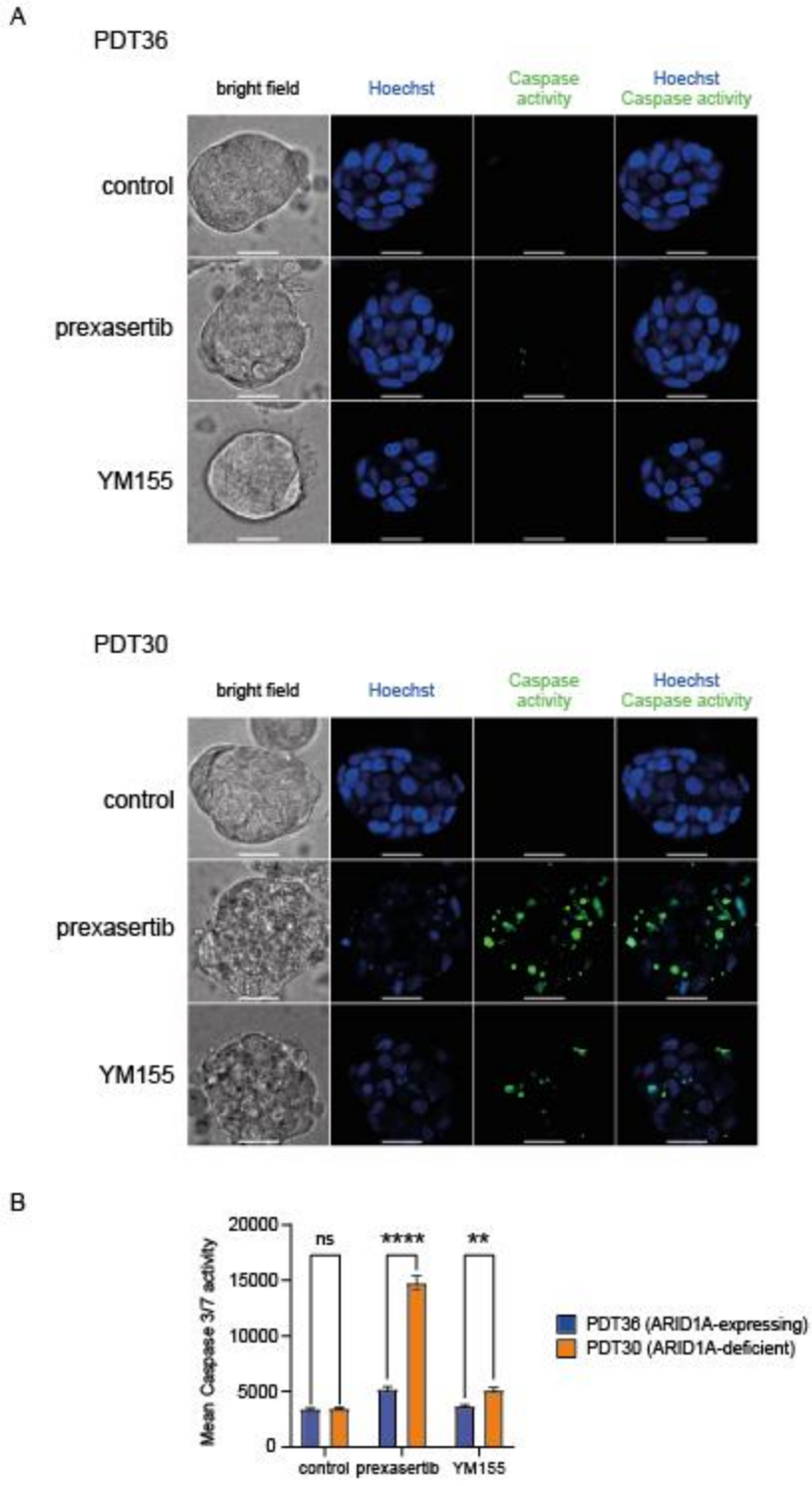

Supplemental Figure 9. A) Representative bright field and fluorescence staining showing caspase 3/7 activity (green) in *ARID1A*-expressing (PDT36) and *ARID1A*-deficient (PDT30) bladder tumoroids treated for 48 hours with 32nM prexasertib or 50nM YM155, compared to untreated controls. Hoechst (blue) was used as a counter staining. **B)** Bar graph depicting mean staining intensity (Caspase 3/7 activity) per

885 tumoroid. At least 49 tumoroids were measured per condition and data are presented as mean +-SEM.
886 **P<0.005, ****P<0.00005.

887

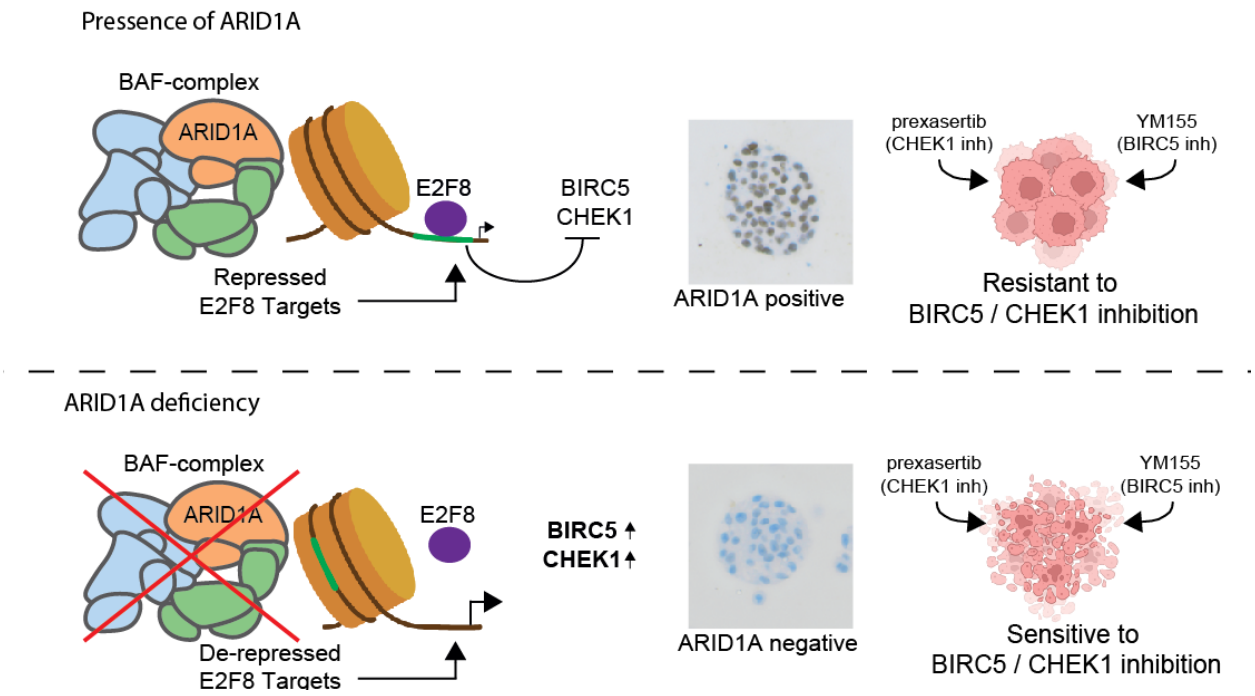

Supplemental Figure 10. Theoretical model for the interaction of E2F8 and ARID1A and regulation of CHEK1 and BIRC5 expression in ARID1A-expressing and ARID1A-deficient cells. Top: ARID1A and the BAF complex reposition the nucleosome, exposing E2F8 binding motifs. Upon binding, E2F8 represses its target genes, including CHEK1 and BIRC5. As a result, CHEK1 and BIRC5 expression is generally repressed, making ARID1A-expressing cells relatively resistant to BIRC5 and CHEK1 inhibition. **Bottom:** Loss of ARID1A expression disrupts the BAF complex's ability to reposition nucleosomes, hindering E2F8 binding and leading to de-repression of BIRC5 and CHECK1. In turn, upregulated expression of BIRC5 and CHEK1 can be therapeutically targeted by small molecule inhibitors, thereby selectively eliminating *ARID1A*-deficient BC cells.

REFERENCES

1. Sung H, Ferlay J, Siegel RL, Laversanne M, Soerjomataram I, Jemal A, Bray F: **Global Cancer Statistics 2020: GLOBOCAN Estimates of Incidence and Mortality Worldwide for 36 Cancers in 185 Countries.** *CA: A Cancer Journal for Clinicians* 2021, **71:**209-249.
2. Alfred Witjes J, Max Bruins H, Carrión A, Cathomas R, Compérat E, Efstathiou JA, Fietkau R, Gakis G, Lorch A, Martini A, et al: **European Association of Urology Guidelines on Muscle-invasive and Metastatic Bladder Cancer: Summary of the 2023 Guidelines.** *European Urology* 2024, **85:**17-31.
3. Powles T, Bellmunt J, Comperat E, De Santis M, Huddart R, Loriot Y, Necchi A, Valderrama BP, Ravaud A, Shariat SF, et al: **Bladder cancer: ESMO Clinical Practice Guideline for diagnosis, treatment and follow-up[☆].** *Annals of Oncology* 2022, **33:**244-258.
4. Robertson AG, Kim J, Al-Ahmadie H, Bellmunt J, Guo G, Cherniack AD, Hinoue T, Laird PW, Hoadley KA, Akbani R, et al: **Comprehensive Molecular Characterization of Muscle-Invasive Bladder Cancer.** *Cell* 2017, **171:**540-556.e525.
5. Taber A, Christensen E, Lamy P, Nordentoft I, Prip F, Lindskrog SV, Birkenkamp-Demtröder K, Okholm TLH, Knudsen M, Pedersen JS, et al: **Molecular correlates of cisplatin-based chemotherapy response in muscle invasive bladder cancer by integrated multi-omics analysis.** *Nat Commun* 2020, **11:**4858.
6. Damrauer JS, Beckabir W, Klomp J, Zhou M, Plimack ER, Galsky MD, Grivas P, Hahn NM, O'Donnell PH, Iyer G, et al: **Collaborative study from the Bladder Cancer Advocacy Network for the genomic analysis of metastatic urothelial cancer.** *Nature Communications* 2022, **13:**6658.
7. Nakauma-González JA, Rijnders M, van Riet J, van der Heijden MS, Voortman J, Cuppen E, Mehra N, van Wilpe S, Oosting SF, Rijstenberg LL, et al: **Comprehensive Molecular Characterization Reveals Genomic and Transcriptomic Subtypes of Metastatic Urothelial Carcinoma.** *European Urology* 2022, **81:**331-336.
8. Conde M, Frew IJ: **Therapeutic significance of ARID1A mutation in bladder cancer.** *Neoplasia* 2022, **31:**100814.
9. Jana S, Brahma S, Arora S, Wladyka CL, Hoang P, Blinka S, Hough R, Horn JL, Liu Y, Wang LJ, et al: **Transcriptional-translational conflict is a barrier to cellular transformation and cancer progression.** *Cancer Cell* 2023, **41:**853-870.e813.
10. Zhao B, Lin J, Rong L, Wu S, Deng Z, Fatkhutdinov N, Zundell J, Fukumoto T, Liu Q, Kossenkov A, et al: **ARID1A promotes genomic stability through protecting telomere cohesion.** *Nature Communications* 2019, **10:**4067.
11. Shen J, Peng Y, Wei L, Zhang W, Yang L, Lan L, Kapoor P, Ju Z, Mo Q, Shih Ie M, et al: **ARID1A Deficiency Impairs the DNA Damage Checkpoint and Sensitizes Cells to PARP Inhibitors.** *Cancer Discov* 2015, **5:**752-767.
12. Lo YH, Kolahi KS, Du Y, Chang CY, Krokhotin A, Nair A, Sobba WD, Karlsson K, Jones SJ, Longacre TA, et al: **A CRISPR/Cas9-Engineered ARID1A-Deficient Human Gastric Cancer Organoid Model Reveals Essential and Nonessential Modes of Oncogenic Transformation.** *Cancer Discov* 2021, **11:**1562-1581.
13. Katt ME, Placone AL, Wong AD, Xu ZS, Searson PC: **In Vitro Tumor Models: Advantages, Disadvantages, Variables, and Selecting the Right Platform.** *Front Bioeng Biotechnol* 2016, **4:**12.

14. Hidalgo M, Amant F, Biankin AV, Budinská E, Byrne AT, Caldas C, Clarke RB, de Jong S, Jonkers J, Mælandsmo GM, et al: **Patient-derived xenograft models: an emerging platform for translational cancer research.** *Cancer Discov* 2014, **4:**998-1013.
15. Wensink GE, Elias SG, Mullenders J, Koopman M, Boj SF, Kranenburg OW, Roodhart JML: **Patient-derived organoids as a predictive biomarker for treatment response in cancer patients.** *npj Precision Oncology* 2021, **5:**30.
16. Gunti S, Hoke ATK, Vu KP, London NR, Jr.: **Organoid and Spheroid Tumor Models: Techniques and Applications.** *Cancers (Basel)* 2021, **13**.
17. Sato T, Vries RG, Snippert HJ, van de Wetering M, Barker N, Stange DE, van Es JH, Abo A, Kujala P, Peters PJ, Clevers H: **Single Lgr5 stem cells build crypt-villus structures in vitro without a mesenchymal niche.** *Nature* 2009, **459:**262-265.
18. Minoli M, Cantore T, Hanhart D, Kiener M, Fedrizzi T, La Manna F, Karkampouna S, Chouvardas P, Genitsch V, Rodriguez-Calero A, et al: **Bladder cancer organoids as a functional system to model different disease stages and therapy response.** *Nat Commun* 2023, **14:**2214.
19. Lee SH, Hu W, Matulay JT, Silva MV, Owczarek TB, Kim K, Chua CW, Barlow LJ, Kandoth C, Williams AB, et al: **Tumor Evolution and Drug Response in Patient-Derived Organoid Models of Bladder Cancer.** *Cell* 2018, **173:**515-528.e517.
20. Mullenders J, de Jongh E, Brousali A, Roosen M, Blom JPA, Begthel H, Korving J, Jonges T, Kranenburg O, Meijer R, Clevers HC: **Mouse and human urothelial cancer organoids: A tool for bladder cancer research.** *Proc Natl Acad Sci U S A* 2019, **116:**4567-4574.
21. Mastri M, Ramakrishnan S, Shah SD, Karasik E, Gillard BM, Moser MT, Farmer BK, Azabdaftari G, Chatta GS, Woloszynska A, et al: **Patient derived models of bladder cancer enrich the signal of the tumor cell transcriptome facilitating the analysis of the tumor cell compartment.** *Am J Clin Exp Urol* 2021, **9:**416-434.
22. Wiegand KC, Shah SP, Al-Agha OM, Zhao Y, Tse K, Zeng T, Senz J, McConechy MK, Anglesio MS, Kalloger SE, et al: **ARID1A mutations in endometriosis-associated ovarian carcinomas.** *N Engl J Med* 2010, **363:**1532-1543.
23. Minoche AE, Lundie B, Peters GB, Ohnesorg T, Pinese M, Thomas DM, Zankl A, Roscioli T, Schonrock N, Kummerfeld S, et al: **ClinSV: clinical grade structural and copy number variant detection from whole genome sequencing data.** *Genome Medicine* 2021, **13:**32.
24. Zhao B, Lin J, Rong L, Wu S, Deng Z, Fatkhutdinov N, Zundell J, Fukumoto T, Liu Q, Kossenkov A, et al: **ARID1A promotes genomic stability through protecting telomere cohesion.** *Nat Commun* 2019, **10:**4067.
25. van Oers JM, Lurkin I, van Exsel AJ, Nijsen Y, van Rhijn BW, van der Aa MN, Zwarthoff EC: **A simple and fast method for the simultaneous detection of nine fibroblast growth factor receptor 3 mutations in bladder cancer and voided urine.** *Clin Cancer Res* 2005, **11:**7743-7748.
26. Hurst CD, Zuiverloon TCM, Hafner C, Zwarthoff EC, Knowles MA: **A SNaPshot assay for the rapid and simple detection of four common hotspot codon mutations in the PIK3CA gene.** *BMC Research Notes* 2009, **2:**66.
27. Allory Y, Beukers W, Sagrera A, Flández M, Marqués M, Márquez M, van der Keur KA, Dyrskjot L, Lurkin I, Vermeij M, et al: **Telomerase Reverse Transcriptase Promoter Mutations in Bladder Cancer: High Frequency Across Stages, Detection in Urine, and Lack of Association with Outcome.** *European Urology* 2014, **65:**360-366.
28. Hanahan D, Weinberg Robert A: **Hallmarks of Cancer: The Next Generation.** *Cell* 2011, **144:**646-674.
29. Jana S, Brahma S, Arora S, Wladyka CL, Hoang P, Blinka S, Hough R, Horn JL, Liu Y, Wang L-J, et al: **Transcriptional-translational conflict is a barrier to cellular transformation and cancer progression.** *Cancer Cell* 2023, **41:**853-870.e813.

30. Trimarchi JM, Lees JA: **Sibling rivalry in the E2F family.** *Nature Reviews Molecular Cell Biology* 2002, **3:**11-20.
31. Stevens C, La Thangue NB: **The emerging role of E2F-1 in the DNA damage response and checkpoint control.** *DNA Repair* 2004, **3:**1071-1079.
32. DeGregori J, Johnson DG: **Distinct and Overlapping Roles for E2F Family Members in Transcription, Proliferation and Apoptosis.** *Curr Mol Med* 2006, **6:**739-748.
33. Lammens T, Li J, Leone G, De Veylder L: **Atypical E2Fs: new players in the E2F transcription factor family.** *Trends in Cell Biology* 2009, **19:**111-118.
34. Morgunova E, Yin Y, Jolma A, Dave K, Schmierer B, Popov A, Eremina N, Nilsson L, Taipale J: **Structural insights into the DNA-binding specificity of E2F family transcription factors.** *Nature Communications* 2015, **6:**10050.
35. Luo Y, Hitz BC, Gabdank I, Hilton JA, Kagda MS, Lam B, Myers Z, Sud P, Jou J, Lin K, et al: **New developments on the Encyclopedia of DNA Elements (ENCODE) data portal.** *Nucleic Acids Res* 2020, **48:**D882-d889.
36. Nakauma-González JA, Rijnders M, Noordsij MTW, Martens JWM, van der Veldt AAM, Lolkema MPJ, Boormans JL, van de Werken HJG: **Whole-genome mapping of APOBEC mutagenesis in metastatic urothelial carcinoma identifies driver hotspot mutations and a novel mutational signature.** *Cell Genomics* 2024, **4:**100528.
37. Carmena M, Wheelock M, Funabiki H, Earnshaw WC: **The chromosomal passenger complex (CPC): from easy rider to the godfather of mitosis.** *Nature Reviews Molecular Cell Biology* 2012, **13:**789-803.
38. Bartek J, Lukas J: **Chk1 and Chk2 kinases in checkpoint control and cancer.** *Cancer Cell* 2003, **3:**421-429.
39. Shimizu T, Nishio K, Sakai K, Okamoto I, Okamoto K, Takeda M, Morishita M, Nakagawa K: **Phase I safety and pharmacokinetic study of YM155, a potent selective survivin inhibitor, in combination with erlotinib in patients with EGFR TKI refractory advanced non-small cell lung cancer.** *Cancer Chemotherapy and Pharmacology* 2020, **86:**211-219.
40. Tolcher AW, Quinn DI, Ferrari A, Ahmann F, Giaccone G, Drake T, Keating A, de Bono JS: **A phase II study of YM155, a novel small-molecule suppressor of survivin, in castration-resistant taxane-pretreated prostate cancer.** *Annals of Oncology* 2012, **23:**968-973.
41. Papadopoulos KP, Lopez-Jimenez J, Smith SE, Steinberg J, Keating A, Sasse C, Jie F, Thyss A: **A multicenter phase II study of sepantronium bromide (YM155) plus rituximab in patients with relapsed aggressive B-cell Non-Hodgkin lymphoma.** *Leukemia and Lymphoma* 2016, **57:**1848-1855.
42. Nakahara T, Kita A, Yamanaka K, Mori M, Amino N, Takeuchi M, Tominaga F, Hatakeyama S, Kinoyama I, Matsuhisa A, et al: **YM155, a novel small-molecule survivin suppressant, induces regression of established human hormone-refractory prostate tumor xenografts.** *Cancer Res* 2007, **67:**8014-8021.
43. **News Release Details, Acrivon Therapeutics Announces FDA Grants Fast Track Designation for Development of ACR-368 in Platinum-Resistant Ovarian Cancer and Endometrial Cancer.** *https://iracrivoncom/news-releases/news-release-details/acrivon-therapeutics-announces-fda-grants-fast-track-designation* 2023.
44. Jiang T, Chen X, Su C, Ren S, Zhou C: **Pan-cancer analysis of ARID1A Alterations as Biomarkers for Immunotherapy Outcomes.** *J Cancer* 2020, **11:**776-780.
45. Bass AJ, Thorsson V, Shmulevich I, Reynolds SM, Miller M, Bernard B, Hinoue T, Laird PW, Curtis C, Shen H, et al: **Comprehensive molecular characterization of gastric adenocarcinoma.** *Nature* 2014, **513:**202-209.

46. Ogiwara H, Takahashi K, Sasaki M, Kuroda T, Yoshida H, Watanabe R, Maruyama A, Makinoshima H, Chiwaki F, Sasaki H, et al: **Targeting the Vulnerability of Glutathione Metabolism in ARID1A-Deficient Cancers.** *Cancer Cell* 2019, **35:**177-190.e178.
47. Bitler BG, Aird KM, Garipov A, Li H, Amatangelo M, Kossenkov AV, Schultz DC, Liu Q, Shih Ie M, Conejo-Garcia JR, et al: **Synthetic lethality by targeting EZH2 methyltransferase activity in ARID1A-mutated cancers.** *Nat Med* 2015, **21:**231-238.
48. Kim KH, Kim W, Howard TP, Vazquez F, Tsherniak A, Wu JN, Wang W, Haswell JR, Walensky LD, Hahn WC, et al: **SWI/SNF-mutant cancers depend on catalytic and non-catalytic activity of EZH2.** *Nat Med* 2015, **21:**1491-1496.
49. Lo YH, Karlsson K, Kuo CJ: **Applications of Organoids for Cancer Biology and Precision Medicine.** *Nat Cancer* 2020, **1:**761-773.
50. Minoli M, Cantore T, Hanhart D, Kiener M, Fedrizzi T, La Manna F, Karkampouna S, Chouvardas P, Genitsch V, Rodriguez-Calero A, et al: **Bladder cancer organoids as a functional system to model different disease stages and therapy response.** *Nature Communications* 2023, **14:**2214.
51. Garioni M, Tschan VJ, Blukacz L, Nuciforo S, Parmentier R, Roma L, Coto-Llerena M, Pueschel H, Piscuoglio S, Vlajnic T, et al: **Patient-derived organoids identify tailored therapeutic options and determinants of plasticity in sarcomatoid urothelial bladder cancer.** *npj Precision Oncology* 2023, **7:**112.
52. Santos CP, Lapi E, Martínez de Villarreal J, Álvaro-Espinosa L, Fernández-Barral A, Barbáchano A, Domínguez O, Laughney AM, Megías D, Muñoz A, Real FX: **Urothelial organoids originating from Cd49f(high) mouse stem cells display Notch-dependent differentiation capacity.** *Nat Commun* 2019, **10:**4407.
53. de Witte CJ, Espejo Valle-Inclan J, Hami N, Lõhmussaar K, Kopper O, Vreuls CPH, Jonges GN, van Diest P, Nguyen L, Clevers H, et al: **Patient-Derived Ovarian Cancer Organoids Mimic Clinical Response and Exhibit Heterogeneous Inter- and Intrapatient Drug Responses.** *Cell Rep* 2020, **31:**107762.
54. Vlachogiannis G, Hedayat S, Vatsiou A, Jamin Y, Fernández-Mateos J, Khan K, Lampis A, Eason K, Huntingford I, Burke R, et al: **Patient-derived organoids model treatment response of metastatic gastrointestinal cancers.** *Science* 2018, **359:**920-926.
55. Yao Y, Xu X, Yang L, Zhu J, Wan J, Shen L, Xia F, Fu G, Deng Y, Pan M, et al: **Patient-Derived Organoids Predict Chemoradiation Responses of Locally Advanced Rectal Cancer.** *Cell Stem Cell* 2020, **26:**17-26.e16.
56. Matano M, Date S, Shimokawa M, Takano A, Fujii M, Ohta Y, Watanabe T, Kanai T, Sato T: **Modeling colorectal cancer using CRISPR-Cas9-mediated engineering of human intestinal organoids.** *Nat Med* 2015, **21:**256-262.
57. Drost J, van Jaarsveld RH, Ponsioen B, Zimberlin C, van Boxtel R, Buijs A, Sachs N, Overmeer RM, Offerhaus GJ, Begthel H, et al: **Sequential cancer mutations in cultured human intestinal stem cells.** *Nature* 2015, **521:**43-47.
58. Nanki K, Toshimitsu K, Takano A, Fujii M, Shimokawa M, Ohta Y, Matano M, Seino T, Nishikori S, Ishikawa K, et al: **Divergent Routes toward Wnt and R-spondin Niche Independency during Human Gastric Carcinogenesis.** *Cell* 2018, **174:**856-869.e817.
59. Nagl NG, Jr., Wang X, Patsialou A, Van Scoy M, Moran E: **Distinct mammalian SWI/SNF chromatin remodeling complexes with opposing roles in cell-cycle control.** *Embo j* 2007, **26:**752-763.
60. Sun X, Wang SC, Wei Y, Luo X, Jia Y, Li L, Gopal P, Zhu M, Nassour I, Chuang J-C, et al: **Arid1a Has Context-Dependent Oncogenic and Tumor Suppressor Functions in Liver Cancer.** *Cancer Cell* 2017, **32:**574-589.e576.

61. Nagl NG, Jr., Patsialou A, Haines DS, Dallas PB, Beck GR, Jr., Moran E: **The p270 (ARID1A/SMARCF1) subunit of mammalian SWI/SNF-related complexes is essential for normal cell cycle arrest.** *Cancer Res* 2005, **65:**9236-9244.
62. Xing T, Li L, Rao X, Zhao J, Chen Y, Ju G, Xu Y, Gao X, Dong G, Xia X, et al: **ARID1A deficiency promotes progression and potentiates therapeutic antitumour immunity in hepatitis B virus-related hepatocellular carcinoma.** *BMC Gastroenterology* 2024, **24:**11.
63. Santos A, Wernersson R, Jensen LJ: **Cyclebase 3.0: a multi-organism database on cell-cycle regulation and phenotypes.** *Nucleic Acids Res* 2015, **43:**D1140-1144.
64. Boekhout M, Yuan R, Wondergem AP, Segeren HA, van Liere EA, Awol N, Jansen I, Wolthuis RM, de Bruin A, Westendorp B: **Feedback regulation between atypical E2Fs and APC/CCdh1 coordinates cell cycle progression.** *EMBO Rep* 2016, **17:**414-427.
65. Yuan R, Vos HR, van Es RM, Chen J, Burgering BM, Westendorp B, de Bruin A: **Chk1 and 14-3-3 proteins inhibit atypical E2Fs to prevent a permanent cell cycle arrest.** *Embo j* 2018, **37**.
66. Watanabe R, Ui A, Kanno S-i, Ogiwara H, Nagase T, Kohno T, Yasui A: **SWI/SNF Factors Required for Cellular Resistance to DNA Damage Include ARID1A and ARID1B and Show Interdependent Protein Stability.** *Cancer Research* 2014, **74:**2465-2475.
67. Park JH, Park EJ, Lee HS, Kim SJ, Hur SK, Imbalzano AN, Kwon J: **Mammalian SWI/SNF complexes facilitate DNA double-strand break repair by promoting gamma-H2AX induction.** *Embo J* 2006, **25:**3986-3997.
68. Williamson CT, Miller R, Pemberton HN, Jones SE, Campbell J, Konde A, Badham N, Rafiq R, Brough R, Gulati A, et al: **ATR inhibitors as a synthetic lethal therapy for tumours deficient in ARID1A.** *Nat Commun* 2016, **7:**13837.
69. Dykhuizen EC, Hargreaves DC, Miller EL, Cui K, Korshunov A, Kool M, Pfister S, Cho YJ, Zhao K, Crabtree GR: **BAF complexes facilitate decatenation of DNA by topoisomerase IIα.** *Nature* 2013, **497:**624-627.
70. Konstantinopoulos PA, Lee JM, Gao B, Miller R, Lee JY, Colombo N, Vergote I, Credille KM, Young SR, McNeely S, et al: **A Phase 2 study of prexasertib (LY2606368) in platinum resistant or refractory recurrent ovarian cancer.** *Gynecol Oncol* 2022, **167:**213-225.
71. Naldini L, Blömer U, Gage FH, Trono D, Verma IM: **Efficient transfer, integration, and sustained long-term expression of the transgene in adult rat brains injected with a lentiviral vector.** *Proceedings of the National Academy of Sciences* 1996, **93:**11382.
72. Kim D, Paggi JM, Park C, Bennett C, Salzberg SL: **Graph-based genome alignment and genotyping with HISAT2 and HISAT-genotype.** *Nat Biotechnol* 2019, **37:**907-915.
73. Langmead B, Salzberg SL: **Fast gapped-read alignment with Bowtie 2.** *Nat Methods* 2012, **9:**357-359.
74. Fanidis D, Moulos P: **Integrative, normalization-insusceptible statistical analysis of RNA-Seq data, with improved differential expression and unbiased downstream functional analysis.** *Briefings in Bioinformatics* 2020, **22**.
75. Love MI, Huber W, Anders S: **Moderated estimation of fold change and dispersion for RNA-seq data with DESeq2.** *Genome Biology* 2014, **15:**550-550.
76. Yu G, He QY: **ReactomePA: An R/Bioconductor package for reactome pathway analysis and visualization.** *Molecular BioSystems* 2016, **12:**477-479.
77. Therneau T: **A Package for Survival Analysis in R. R package version 3.6-4.** *https://CRANR-projectorg/package=survival* 2024.
78. Team RC: **R Core Team (2017). R: A language and environment for statistical computing.** *R Foundation for Statistical Computing, Vienna, Austria URL http://wwwR-projectorg/* 2017:R Foundation for Statistical Computing-R Foundation for Statistical Computing.

1130